

Structural and Metamorphic History of the Leech River Shear Zone, Vancouver Island, British Columbia

C. Seyler, J. Kirkpatrick, C. Faber, Alexis Licht, D. Šilerová, C. Regalla

▶ **To cite this version:**

C. Seyler, J. Kirkpatrick, C. Faber, Alexis Licht, D. Šilerová, et al.. Structural and Metamorphic History of the Leech River Shear Zone, Vancouver Island, British Columbia. Tectonics, 2022, 41 (11), 10.1029/2021TC007132 . hal-03867718

HAL Id: hal-03867718
https://hal.science/hal-03867718

Submitted on 23 Nov 2022

HAL is a multi-disciplinary open access archive for the deposit and dissemination of scientific research documents, whether they are published or not. The documents may come from teaching and research institutions in France or abroad, or from public or private research centers.

L'archive ouverte pluridisciplinaire **HAL**, est destinée au dépôt et à la diffusion de documents scientifiques de niveau recherche, publiés ou non, émanant des établissements d'enseignement et de recherche français ou étrangers, des laboratoires publics ou privés.

Structural and metamorphic history of the Leech River Shear Zone, Vancouver Island, British Columbia

C. E. Seyler[1†*], J. D. Kirkpatrick[1], C. Faber[2], A. Licht[3,4], D. Šilerová[1‡], and C. Regalla[5]

[1]Department of Earth and Planetary Sciences, McGill University, Montréal, QC, Canada

[2]Department of Geosciences, UiT The Arctic University of Norway, Tromsø, Norway

[3]Aix-Marseille Université, CNRS, Centre de Recherche et d'Enseignement de Géosciences de l'Environnement (CEREGE), Aix-en-Provence, France

[4]Department of Earth and Space Sciences, University of Washington, Seattle, WA, USA

[5]School of Earth and Sustainability, Northern Arizona University, Flagstaff, AZ, USA

[†]Now at University of Texas Institute for Geophysics and Department of Geological Sciences, University of Texas, Austin, TX, USA

[‡]Now at Department of Earth Sciences, Simon Fraser University, Burnaby, BC, Canada

* *Corresponding author*: Caroline Seyler (caroline.seyler@utexas.edu)

Key Points

- Leech River Shear Zone confirmed as a hot, Eocene-age paleo-subduction interface
- High-temperature metamorphism produced by ridge subduction during accretion of Siletz-Crescent terrane
- New detrital zircon ages from the Leech River Schist support near-trench deposition during Paleocene

Abstract

The Leech River Shear Zone (LRSZ) on southern Vancouver Island separates the metasedimentary schists of the Leech River Complex from the accreted oceanic plateau of the Siletz-Crescent terrane. The juxtaposition of these rock units suggests a possible origin as a

subduction plate boundary, but tectonic context of the LRSZ has yet to be fully established. We present field, microstructural, petrological, and geochronological observations that constrain the structural and metamorphic history of LRSZ. The mylonite zone of the LRSZ straddles the lithologic contact between the schists of the Leech River Complex and basalts of the Siletz-Crescent terrane. Foliation orientations, a steeply plunging stretching lineation, and kinematic indicators all suggest reverse-sinistral motion. Compositions of garnet in the schist and amphibole in the metabasalt record syn-kinematic growth at temperature and pressure conditions of 550–570 °C and 450–490 MPa. These metamorphic conditions require elevated geotherms that are consistent with plate models that position the Kula-Farallon Ridge and Yellowstone Hotspot in the region in the Eocene (~50 Ma). Detrital zircon U-Pb age distributions for the Leech River Schist have Paleocene maximum depositional ages and are similar to the Upper Nanaimo Group that unconformably overlies the Wrangellia terrane. Our ages support early Paleocene deposition of the schist in a subduction trench/slope environment followed by underthrusting and underplating. These results establish the exhumed mylonite zone of the LRSZ as a paleo-plate interface that was active during Eocene subduction.

1 Introduction

Subduction zone dynamics are strongly influenced by the mechanical properties of subduction interface shear zones (Behr et al., 2022). However, the relevant properties of subduction interfaces, such as their widths, rock types, and internal structure, cannot be determined via geophysical observation. Instead, field- and micro-scale observations of exhumed shear zones that were active during subduction are needed to fill this knowledge gap. Subduction dynamics and thermal gradients evolve as they mature (e.g., Holt & Condit, 2021), and subduction zones can encompass a broad range of environments (Chelle-Michou et al., 2022), for example, when influenced by atypical subduction geometries like ridge subduction (e.g., DeLong et al., 1979; Sakaguchi, 1996; Brown, 1998). A more complete inventory capturing the variability of subduction interfaces is therefore needed to better understand their behavior.

The Canadian Cordillera potentially exposes numerous subduction-related structures as it was assembled through a series of accretionary orogenies. One candidate structure is the Leech River Fault (Fig. 1), a terrane-bounding fault located on southern Vancouver Island in British

Columbia that juxtaposes mafic volcanic and igneous rocks of the Metchosin Igneous Complex (MIC) to the south with the predominantly metapelitic Leech River Complex (LRC). For clarity, we will term this structure the "Leech River Shear Zone" (LRSZ) to differentiate it from the recently active "Leech River Fault", which is locally coincident (Morrell et al., 2017, 2018; Li et al., 2018; Harrichhausen et al., 2021). The MIC is part of the Siletz-Crescent terrane, a ~10–30 km-thick sequence of Eocene mafic volcanics and intrusive suites that extends from Vancouver Island to Oregon. Trace element and rare earth element geochemistry of basalts from the terrane (Phillips et al., 2017), combined with the terrane's thickness (Clowes et al., 1987; Tréhu et al., 1994), indicate the Siletz-Crescent terrane represents a portion of a large igneous province that formed on the Farallon plate, near the Kula/Resurrection-Farallon ridge, and above a mantle plume, potentially the Yellowstone Hotspot (Wells et al., 2014; Phillips et al., 2017). Accretion of the Siletz-Crescent terrane is therefore inferred to have occurred during subduction and impacted the deformation of the subduction forearc and tectonics of the upper plate (Eddy et al., 2016).

Previous work on the LRSZ presents conflicting interpretations of the tectonic context of this structure. Seismic reflection images show the contact between the LRC and MIC extends from the surface trace of the LRSZ, and dips to the north under Vancouver Island and projects to the surface trace of the LRSZ (Clowes et al., 1987; Matharu et al., 2014). Combined with the ages of the LRC (Cretaceous; Groome et al., 2003) and MIC (Eocene; Duncan, 1982; McCrory & Wilson, 2013), this geometry suggests the LRSZ hosted reverse-sense motion, consistent with formation in a subduction setting. However, previous field data suggests dominantly strike-slip motion (Fairchild & Cowan, 1982; Groome, 2000), possibly related to development of a forearc rift basin formed on the continental margin, which was previously proposed as the tectonic origin of the MIC (Babcock et al., 1992; Wells et al., 1984). The origin of the LRC is also uncertain due to the lack of a depositional age and its previous interpretation as allochthonous to Vancouver Island (Fairchild & Cowan, 1982).

In this study, we use structural, petrological, and geochronological data to re-evaluate the tectonic origin of the LRSZ and the LRC. We directly tested the thrust vs. strike-slip faulting regime with field and microstructural observations that establish the kinematics of deformation.

We probed mineral compositions (garnet and amphibole), applied the Ti-in-biotite geothermometer, and conducted phase equilibrium modeling to develop metamorphic histories for the shear zone rocks and determine the syn-kinematic P-T conditions. We also measured the U-Pb dates of detrital zircons from the LRC to determine its depositional age and setting. Our results provide the first constraints on the paleogeographic and tectonic origin of the LRC and the syn-kinematic pressure, temperature, and timing of deformation on the LRSZ. The results indicate that the LRSZ was an Eocene-age, hot subduction interface that formed during underthrusting of the Siletz-Crescent terrane beneath the previously underplated LRC as the Farallon plate subducted under North America.

2 Geologic setting

The LRSZ is an east-west trending, terrane-bounding structure that separates the Leech River Complex (LRC) north of the fault from the Metchosin Igneous Complex (MIC) to the south. The LRC, together with the Pandora Peak Unit and Pacific Rim Complex, collectively make up the Pacific Rim terrane, a southern correlative of the Chugach-Prince William accretionary complexes in Alaska (Cowan, 2003; Cowan et al., 1997; Garver & Davidson, 2015). The MIC, the Crescent Formation of Washington, the Coast Range Volcanic Province of Washington and Oregon, and the Siletz River Volcanics of Oregon comprise the Siletz-Crescent terrane (Duncan, 1982; Irving, 1979; McCrory & Wilson, 2013; Simpson & Cox, 1977).

2.1 Leech River Shear Zone

The LRSZ has been previously reported as a fault zone with two to four discrete left-lateral strike slip faults, lacking any fault gouge, breccia, or mylonitization (Fairchild & Cowan, 1982) as well as a left-lateral shear zone composed of mylonites ("Bear Creek Shear Zone" in Groome, 2000). The interpretation of the LRSZ as a left-lateral strike slip fault was largely based on the regional steep dip of the fault (Fairchild & Cowan, 1982). Limited observations of shear sense indicators from mylonites within the Bear Creek Shear Zone indicate left-lateral motion (Groome, 2000). Quaternary reactivation of this structure as a wide zone of strike-slip faults has been documented through identification of fault scarps (Morell et al., 2017), microseismicity (Li et al., 2018), and paleoseismic trenching (Morell et al., 2018; Harrichhausen et al., 2021). Here, we focus on the ancient structure that established the tectonic contact between the LRC and MIC (the “Leech

River Shear Zone"), rather than the recently active "Leech River Fault", which is locally parallel and co-located with the terrane boundary and mylonite zone of the LRSZ

2.2 Leech River Complex

The LRC is an approximately 10 km-thick package of metasedimentary rocks that crop out in an east-west trending unit on southern Vancouver Island (Fig. 1). The LRC is bounded to the north by the San Juan and Survey Mountain faults, which juxtapose the LRC with the Wrangellia terrane and the Pandora Peak Unit of the Pacific Rim terrane, respectively (Rusmore & Cowan, 1985). The LRC includes the Leech River Schist (LRS), the Jordan River Unit, the Tripp Creek Metabasite, and the Walker Creek intrusions (Fairchild & Cowan, 1982).

The LRS is a metapelitic schist containing metapsammitic layers. Based on the assemblage of discontinuous layers of metamorphosed shales and sandstones with minor chert and basaltic volcanics, the LRS was interpreted as a submarine, near-continental margin turbidite sequence deposited near a source of basalt, such as a spreading ridge (Fairchild & Cowan, 1982; Muller, 1977b, 1980). The LRS has a reported maximum depositional age of 103 Ma derived from the youngest detrital zircon dated by Groome et al. (2003). Fairchild and Cowan (1982) reported transposed sedimentary layering, aligned metapsammitic lenses within a metapelitic matrix, and two generations of folds with strong axial planar foliation parallel to the compositional layering. These features were interpreted to result from regional north-south shortening (Fairchild & Cowan, 1982). The metamorphic grade of the LRS increases from greenschist facies in the north (chlorite-white mica-biotite phyllites), to amphibolite facies in the south (garnet-staurolite-andalusite schists), and metamorphism was syn- to post-kinematic with regional deformation (Fairchild & Cowan, 1982; Rusmore & Cowan, 1985; Groome et al., 2003). Previous work indicated that the metamorphic gradient was isobaric based on the progression of metamorphic assemblages through a series of east-west isograds for biotite, garnet, staurolite, and andalusite (Rusmore & Cowan, 1985). Estimates of peak pressure (< 350 MPa) and temperature (500–600 °C) are attributed to the presence of andalusite in the southern region within contact aureoles around intrusive units (Rusmore, 1982; Groome et al., 2003).

The Jordan River Unit is a quartz-feldspar-biotite schist that has been interpreted as both the largest body of metasandstone in the LRS (i.e., the Valentine metasandstone in Fairchild & Cowan, 1982; Muller, 1980), and as a plagioclase-rich peraluminous metagranodiorite intrusion derived from anatexis of the LRS with a titanite U-Pb crystallization age of 88 Ma (Groome et al., 2003). The Tripp Creek Metabasite is an actinolite-plagioclase-quartz-garnet schist interpreted as an intrusive unit due to the presence of foliated LRS xenoliths (Groome et al., 2003). The Jordan River Unit and Tripp Creek Metabasite have a schistosity parallel to the foliation in the LRS, suggesting their formation is pre- to syn-kinematic with deformation of the complex. The Walker Creek intrusions are a suite of tonalite, trondhjemite, and granodiorite dikes and sills present in the southern portion of the LRS. Deformation of these intrusions is non-uniform, with some dikes displaying schistosity parallel to the foliation in the LRS while others remain undeformed, suggesting syn- to post-kinematic magmatism (Groome et al., 2003). These intrusions have zircon U-Pb crystallization ages ranging from 51-47 Ma, and their geochemical signatures suggest they are derived from anatexis of the LRS (Groome et al., 2003).

2.3 Metchosin Igneous Complex

The MIC consists of a 3 km-thick ophiolitic pseudostratigraphy consisting of gabbro stocks (Sooke Gabbros), sheeted dikes, and a sequence of basalt flows that transitions from submarine to subaerial up-section (Massey, 1986). Whole rock trace element geochemistry is transitional between N-MORB and E-MORB signatures, suggesting both spreading ridge- and mantle plume- related magmatism (Duncan, 1982; Phillips et al., 2017; Timpa et al., 2005). The age of the complex ranges from 58–52 Ma based on $^{40}Ar/^{39}Ar$ fusion dates and U-Pb zircon dates (Duncan, 1982; Massey, 1986; Yorath et al., 1999). Temperature estimates from amphibole compositions and Al^{iv}-in-chlorite geothermometry suggest the metamorphic grade in the complex increases from prehnite-actinolite in the east to amphibolite in the west along a ~5–10 °C/km horizontal gradient (Timpa et al., 2005). This gradient was interpreted as the result of metamorphism during tectonic emplacement of the MIC followed by differential exhumation (Timpa et al., 2005).

Two contrasting origins for the Siletz-Crescent terrane have been proposed: an oceanic plateau (originally proposed by Duncan (1982)), or extensional volcanism in a forearc rift (Babcock et

al., 1992; Wells et al., 1984). However, the revised 55–49 Ma age range for the terrane (Eddy et al., 2017; McCrory & Wilson, 2013; Wells et al., 2014 and references therein), plate reconstruction modeling (McCrory & Wilson, 2013; Wells et al., 2014), and basalt geochemistry (Phillips et al., 2017) suggest that the Siletz-Crescent terrane represents an accreted oceanic plateau that formed near the Kula/Resurrection-Farallon Ridge by a near-ridge mantle plume, most likely the Yellowstone Hotspot (Duncan, 1982; Eddy et al., 2016; Eddy et al., 2017; McCrory & Wilson, 2013; Phillips et al., 2017; Wells et al., 2014). Shortly after its formation, the Washington and Oregon portion of the terrane docked to North America by 51–48 Ma based on the coccolithophores present in the overlying strata (Wells et al., 2014), the sedimentary record of changing paleoflow direction (Eddy et al., 2016), and the age of intrusives (Eddy et al., 2017). On Vancouver Island, the terrane docked prior to 45–42.5 Ma based on $^{40}Ar/^{39}Ar$ cooling ages in mica that record exhumation of the Leech River Schist (Groome et al., 2003), which is inferred to have been due to uplift related to MIC underplating.

3 Methods

3.1 Detrital zircon analysis

Detrital zircon ages were determined for samples of the Leech River Schist, Jordan River Unit, and Walker Creek intrusions (sample locations in Table S1). Detailed data acquisition and reduction protocols are described in Shekut and Licht (2020). Zircons were extracted by heavy mineral separation, including concentration with a Holman-Wilfley™ gravity table, density separation with methylene iodide, and magnetic separation with a Frantz™ Magnetic Barrier separator. Data was collected using a laser-ablation inductively-coupled-plasma mass-spectrometry (LA-ICP-MS), using an iCAP-RQ Quadrupole ICP-MS coupled to an Analyte G2 excimer laser at the University of Washington, using a spot diameter of 25 microns and Plešovice zircons as calibration reference material (Sláma et al., 2008). Data reduction was conducted with *Iolite* (Version 3.5), using their *U_Pb_Geochron4* Data Reduction Scheme to calculate U-Pb dates uncorrected for common lead (Paton et al., 2010). Uncertainties for all samples were calculated using a modified version of the method of Matthews and Guest (2017) that takes into account the impact of ^{207}Pb beam intensity on date uncertainties (Horstwood et al., 2016). The dates used for plotting are $^{206}Pb/^{238}U$ for dates <1400 Ma and $^{207}Pb/^{206}Pb$ for dates >1400 Ma. Dates >300 Ma were screened for concordance using a discordance filter at >20%

discordance (<80% concordance) and >5% reverse discordance (>105% concordance); we used the $^{206}Pb/^{238}U$ vs $^{207}Pb/^{235}U$ ratio to calculate discordance for dates <1300 Ma, and the $^{206}Pb/^{238}U$ vs. $^{207}Pb/^{206}Pb$ ratio for older dates. A subset of zircon grains from each sample were imaged using cathodoluminescence to assess their growth textures (Fig. S1). Maximum depositional ages (MDA) were calculated from the youngest age population of overlapping dates ($n \geq 3$) using the *TuffZirc* application within IsoPlot (Ludwig, 2003).

3.2 Mineral composition analysis

Electron probe micro-analysis (EPMA) was conducted on representative thin sections of the schist and metabasalt mylonites from the LRSZ to determine the syn-kinematic P-T conditions. Polished thin sections were prepared perpendicular to the foliation and parallel or perpendicular to the lineation from oriented samples (Table S1). Mineral compositions were measured with 5 wavelength-dispersive spectrometers on either a JEOL 8900 electron microprobe or Cameca SX100 Five-FE electron microprobe. Garnet compositions were measured on a Cameca microprobe with an accelerating voltage of 15 kV, a beam current of 20 nA, and a beam diameter of 5 µm. Biotite compositions from samples CS15-DR21 and CS15-SW06 were measured on a JEOL microprobe with an accelerating voltage of 15 kV, a beam current of 20 nA, and a beam diameter = 10 µm. Biotite from samples CS18-25 and CS18-32 were measured on a Cameca microprobe with an accelerating voltage of 15 kV, a beam current of 20 nA, and a beam diameter of 5 µm. Amphibole compositions were measured on a Cameca microprobe with an accelerating voltage of 20 kV, a beam current of 4 nA, and a beam diameter of 5 µm. Amphibole compositions were calculated based on the recommendations and classification scheme approved by the Commission on New Minerals Nomenclature and Classification (CNMNC) of the International Mineralogical Association (Hawthorne et al., 2012; Locock, 2014). Plagioclase compositions were measured on a Cameca microprobe with an accelerating voltage of 15 kV, a beam current of 20 nA, and a beam diameter of 5 µm. Bulk rock compositions were determined by Actlabs using whole rock fusion X-ray fluorescence (XRF) analysis. Phase equilibrium modeling was conducted with *PerpleX* software (version 6.9.9; Connolly, 2005) using the internally consistent dataset of Holland and Powell (1998, revised 2004).

4 Field observations of the hanging wall and footwall

In this section, we describe the LRS to the north and MIC to the south to differentiate the deformation associated with the shear zone from regional structures. Our study area extends from the western coast of the island to the Diversion and Bear Creek reservoirs (Fig. 1). Exposures are best along the coast, in road cuts along Highway 14 and logging roads north of the reservoirs, and around the shores of the reservoirs. Elsewhere, the exposure is very poor due to dense vegetation and till cover. Targeted field sites include Botany Bay (LRS), north of the reservoirs (LRS), and Sombrio Point (Metchosin Basalt).

4.1 Leech River Schist (hanging wall of the LRSZ)

The structural fabrics and metamorphic grade of the Leech River Schist vary throughout the unit. We describe the schist in two localities to illustrate this variability: a ~0.5 km^2 area around Botany Bay located ~5 km north of the mapped trace of the LRSZ (projected offshore), and north of the Diversion and Bear Creek reservoirs, a transect from the northern edge of the high strain zone up to ~2 km north of the LRSZ.

At Botany Bay, the schist is characterized by a block-in-matrix fabric with quartz- and plagioclase-rich metapsammitic blocks hosted in a phyllosilicate-rich metapelitic matrix (Fig. 2a–d). Some larger blocks contain evidence for graded bedding and crossbeds indicating that the lithologic variation represents primary sedimentary bedding (S_0), which included interbedded sand-, silt-, and clay-sized layers. The present-day layer discontinuity and strong deformation fabrics in the matrix, including solution cleavage, imply that bedding was tectonically disrupted and transposed into the block-in-matrix fabric. Block sizes range from centimeter- to meter-scale and larger blocks commonly contain quartz veins that terminate at the block edges. Two foliation orientations are present, with the dominant foliation (S_1) defined by parallel long axes of blocks forming an apparent layering that is parallel to a continuous cleavage in the metapelitic matrix. A less pronounced, spaced cleavage (S_2) in the metapelitic matrix is discordant to the S_1 cleavage (Fig. 2a). Both S_1 and S_2 strike approximately east-west, but S_2 is more steeply dipping, resulting in an intersection lineation that plunges shallowly to the west (Fig. 1c and 3a). Some quartz veins within the blocks are tightly folded with axial surfaces parallel to the S_1 foliation. Asymmetric isoclinal folds of thin metapsammitic blocks intrafolial with S_1 are also observed, which indicate

that S_0 is transposed into S_1 (Fig. 2b). The S_2 foliation is axial planar to tight, asymmetric, disharmonic folding of the S_1 foliation, which exhibits a top-to-the-south vergence direction (Fig. 2c). Later quartz veins crosscut both the blocks and matrix at a low angle to S_1 foliation and are moderately deformed into the S_1 foliation (Fig. 2d). The S_2 foliation is defined by white mica and chlorite, indicating deformation at greenschist conditions (Rusmore, 1982).

North of the Diversion and Bear Creek reservoirs, the schist is characterized by disordered and discontinuous deformation fabrics rather than a block-in-matrix structure (Fig. 2e). The dominant foliation is defined by dismembered compositional layering of metapsammitic and metapelitic layers (millimeters to 2–3 cm-thick), which is transposed and locally parallel to a grain shape preferred orientation of phyllosilicate minerals in the phyllitic layers. The compositional layering is transposed, with an axial planar cleavage. This composite foliation is wavy and irregular, strikes roughly east-west, and dips steeply to the north (Fig. 1d). Asymmetric, tight folds of the layering with parasitic folding are common in both subhorizontal or subvertical sections with top-to-the-west and top-to-the-south vergence, respectively. The similar attitudes of the dominant foliation in this region to the S_2 foliation near Botany Bay, along with the similar vergence direction of asymmetric folds, suggests foliations formed under the same shortening direction. We interpret the dominant foliation north of the reservoirs as an S_2 foliation that has transposed and folded the S_0-S_1 foliation (cf. Fairchild & Cowan, 1982). Quartz veins crosscut the foliation at low and high angles and are often boudinaged and folded with the foliation. Coarse-grained (~1-10 mm) metamorphic minerals of garnet, biotite, staurolite, and andalusite are sometimes present in outcrop, indicating amphibolite grade metamorphism. The foliation is deflected around these grains, suggesting porphyroblast growth was pre- and/or syn-kinematic. Overall, the highly dismembered compositional layers, smaller scale of quartz-plagioclase boudins, and transposition of the S_1 foliation to parallel with S_2 suggests that this region is relatively higher strain compared to the schist at Botany Bay.

4.1.1 Detrital zircon U-Pb

We investigated the origin of the Leech River Complex with detrital zircon geochronology to re-evaluate its depositional age and help determine if the Jordan River Unit is metasedimentary or intrusive. U-Pb ages were analyzed from zircon grains in four samples (sample locations in Fig.

1a): one sample of Walker Creek intrusions, one sample of Leech River Schist, and two samples of the Jordan River Unit, which has been inconsistently described as either a metasandstone (Fairchild & Cowan, 1982; Muller, 1980) or an igneous intrusion (Groome et al., 2003).

The MDA of the Leech River Schist sample is 64.4±2.4 (2σ) Ma and the MDA of the Jordan River samples are 66.9±2.1 Ma and 61.0±2.3 Ma (2σ) (Fig. 3a; Table S3). Zircons in the Leech River Schist and Jordan River metasandstone are detrital, with two significant peaks at 60–100 Ma and 140–200 Ma and a cluster of minor peaks between 1100–1800 Ma. Mesozoic zircons were likely sourced from the nearby Coast Mountains Batholith, the volcanic arc formed from Jurassic-Cretaceous subduction beneath the western margin of Wrangellia (Cecil et al., 2018; Friedman & Armstrong, 1995; Gehrels et al., 2009). Precambrian zircons have several possible sources, which are discussed below. The similar U-Pb age distribution and MDAs for the Leech River Schist and Jordan River Unit, together with petrographic observations (Fig. S2), support the interpretation that the Jordan River Unit is metasedimentary (as defined by Fairchild and Cowan (1982) and Muller (1980)). The Walker Creek intrusion contains very few zircons. The youngest zircon age in the Walker Creek sample is 47.5±1.6 Ma (2σ), which may represent a crystallization age, but this is inconclusive. The Walker Creek age distribution matches distributions from the Leech River Schist and Jordan River metasandstone, suggesting these zircons were all inherited during *in situ* partial melting of the schist, consistent with the peraluminous compositions of the intrusions.

4.2 Metchosin Basalt (footwall of the LRSZ)

The Metchosin Basalt is a very fine-grained to aphanitic amygdaloidal basalt composed of pyroxene or amphibole + plagioclase + epidote + titanite ± chlorite ± quartz. Near Sombrio Point, south of the shear zone, the basalt is massive with preserved volcanic textures, including several meters-scale pillows which contain amygdules. Pillows and pillow interstices contain patches of epidote-rich rock as well as abundant epidote veins (Fig. 2f). There is no grain-scale or distributed foliation, so there is little evidence of pervasive deformation, but small faults with no preferred orientation are observed locally. The lack of consistent deformation fabrics in the basalt away from the LRSZ suggest that the basalt has experienced negligible distributed internal deformation.

5 Field and microstructural observations of the Leech River Shear Zone

In this section, we describe the structure, kinematics, and metamorphism of the LRSZ. Our study area is focused on 10s m^2 exposures predominantly located around the Diversion and Bear Creek reservoirs (Fig. 1), with other exposures located in a region ~12 km along strike toward the coast.

5.1 Structure and kinematics

The LRSZ is an approximately 600-m wide mylonitic shear zone that deformed both the Leech River Schist and the Metchosin Basalt. We define the LRSZ as a high strain zone that contains distinct mylonitic fabrics and kinematic indicators compared to the surrounding rocks. In the schist, the shear zone is characterized by planar and composite foliations, abundant deformed quartz veins, isoclinal folds with subhorizontal and steeply plunging fold axes, and a reduction in grain size (notably of porphyroblasts). In the metabasalt, the shear zone is characterized by planar foliation development and the presence of metamorphic amphibole. The edges of the LRSZ in both lithologies are gradational, and the mylonite zone is wider in the schist than in the metabasalt. The large-scale architecture of the shear zone, including potential lithologic mixing and deformation heterogeneity, is not well constrained due to limited exposure. A lithologic contact between the schist and metabasalt mylonites was only observed in the spillway between the reservoirs, where the contact is sharp and planar over the extent of the outcrop, which is ~10 m in length along strike.

The Leech River Schist mylonite is a strongly foliated and lineated, fine-grained rock (Fig. 4a–e). The mylonitic foliation is sub-parallel to the map-scale structure, striking approximately east-west and dipping steeply (average ~70°) to the north (Fig. 1e). This foliation is defined by subparallel compositional layers, a composite S-C-C’ foliation within phyllosilicate-rich layers, and a ubiquitous grain shape preferred orientation that is locally parallel to the compositional layers (Fig. 1e, 4a–d, and 5a,b). Elongate grains and aggregates of aligned phyllosilicates on foliation planes define a penetrative, steeply plunging stretching lineation (Fig. 1e and 4e). Compositional layers (millimeters to centimeters thick with rare ~10s cm-thick layers) are differentiated by changes in the relative proportion of phyllosilicates, quartz, and feldspar, equivalent to the layering between metapsammitic and metapelitic lithologies north of the shear

zone. These layers are typically planar and continuous for up to tens of centimeters to meters, with lengths limited by boudinage or exposure, such that the layering is extremely attenuated relative to outside the shear zone. Three types of folds affect the layering within the schist mylonite (Fig. 1e). Isoclinal folds of the layering have axial planes parallel to the mylonitic foliation and both sub-horizontal and steeply plunging hinges (Fig. 4b,c). Tight folds of the layering are less common and have axial planes at a low angle to the foliation and steeply plunging axes subparallel to the stretching lineation (Fig. 4f). Kink folds of the foliation are rare and have axial planes at a high angle to the foliation (Fig. 4f). Asymmetry exhibited by all fold types is generally consistent with north-side up reverse shear in subvertical exposures and left-lateral shear in subhorizontal exposures. Shear bands that deflect the layering, boudin margins, and quartz veins define the C-C' composite foliation. We interpret the mylonitic foliation (S_3) to be axial planar to isoclinal folds of $S_{0\text{-}2}$, which are all parallel due to transposition within the shear zone.

The Metchosin metabasalt mylonite contains a strong foliation defined by millimeter- to centimeter-scale compositional layering between plagioclase- and amphibole-rich layers (Fig. 1e and 4g,h). Some compositional layers are boudinaged with boudin long axes parallel to the layering. At the grain-scale, large (~200–500 μm) asymmetric amphibole porphyroblasts are surrounded by a fine-grained amphibole, plagioclase, and sometimes epidote matrix (Fig. 6). Amphibole, plagioclase ribbons, and subparallel trains of titanite and ilmenite grains all show shape-preferred orientations parallel to the compositional layering. Subparallel long axes of amphibole minerals define a steeply plunging, penetrative mineral lineation in the metabasalt mylonite (Fig. 1e).

Quartz veins centimeters to tens of meters long are present in both the schist and metabasalt, though they are far more abundant in the schist mylonite. The range of shapes and attitudes of the veins indicates they were progressively deformed during noncoaxial deformation. Most veins are boudinaged into asymmetric shapes or are isoclinally folded with asymmetric geometries, with axial planes subparallel to the mylonitic foliation and steeply plunging hinges (Fig. 1e and 4). A few veins exhibit folded axial surfaces, indicating they were re-folded and likely formed relatively early in the deformation history. The latest veins are planar and crosscut the foliation at

apparent angles of ~30° in subhorizontal exposures. Large sets of sheeted veins are tens of centimeters to around one meter thick and can be traced for hundreds of meters along strike (Fig. 4a). These sheeted veins are present in both the schist and metabasalt mylonites and contain centimeter-thick layers of quartz separated by sub-millimeter layers of phyllosilicates or amphibole, respectively, interpreted as selvages of the local wall rock. They are also isoclinally folded with steeply dipping axial surfaces subparallel to the mylonitic foliation and are occasionally boudinaged.

Kinematic indicators observed in outcrop (Fig. 4) and in thin section (Fig. 5 and 6) in both the schist and metabasalt mylonites exhibit north-side-up reverse-sense kinematics in steeply dipping exposures and sections (i.e., perpendicular to the foliation and containing the lineation) and apparent sinistral kinematics when viewed in subhorizontal exposures (i.e., perpendicular to the lineation), with reverse-sense indicators most strongly expressed. Overall, the dominant reverse-sense indicators and steeply plunging lineation indicate predominantly thrust motion and secondary sinistral strike-slip motion, which is consistent with sinistral-oblique underthrusting of the Metchosin Basalt beneath the Leech River Schist.

5.2 Pressure and temperature of deformation

Pre- and syn-kinematic P-T conditions were determined with a combination of microstructural observations, mineral chemistry analyses, and phase equilibrium modeling. The schist mylonites in the LRSZ contain garnet + biotite + chlorite + muscovite + plagioclase + quartz + ilmenite ± rutile ± staurolite ± andalusite ± graphite (Fig. 5). Compositional layering between millimeter- to centimeter-thick quartz-plagioclase-rich, and phyllosilicate-rich layers dominates the microstructure (Fig. 5a) with porphyroblasts of garnet, staurolite, and andalusite. Quartz grains exhibit interlobate grain boundaries and subgrain development indicative of crystal-plastic deformation via dislocation creep (Fig. 5b). Garnet occurs within phyllosilicate-rich layers. Garnet porphyroblasts are euhedral, lack evidence of retrogression, and often have weakly asymmetric tails and pressure shadows of quartz and phyllosilicates in both lineation-parallel and lineation-perpendicular orientation (Fig. 5c,d). Some garnet grains are inclusion-free, while others have ilmenite and/or quartz inclusions. Ilmenite grains are also dispersed within mica-dominated layers in the matrix and are aligned with their long axes parallel to foliation. Fine-grained rutile is also present and occurs as elongate grains parallel to the foliation. Andalusite

porphyroblasts (~1–10 mm long) are fragmented, surrounded by reaction rims composed of muscovite and biotite, and have weakly asymmetric tails composed of chlorite, biotite, and muscovite (Fig. 5e). Staurolite porphyroblasts are partially replaced by chlorite and quartz and also have weakly asymmetric tails (Fig. 5f). Biotite porphyroblasts with their basal plane at an angle to the foliation are coarse-grained (~100–1000s µm long), blocky, and often contain graphite interlayers (Fig. 5g). Fine-grained biotite, chlorite, and muscovite are intergrown in phyllosilicate-rich layers with basal planes locally parallel to the foliation. These phyllosilicate-rich layers have variable proportions of each phase, and muscovite-chlorite layers are most common. The reaction rims around andalusite and staurolite porphyroblasts indicate disequilibrium with the matrix phases, and they are therefore likely pre-kinematic with respect to S_3. Some samples show snowball garnets, indicating that garnet, at least partially, grew syn-kinematically with S_3 (Fig. 5d).

Garnet compositions were analyzed to establish the timing of garnet growth and define P-T conditions of metamorphism. Grain transects and compositional maps show zoning in all four garnet components (Fig. 7 and S3; Table S4). Spessartine content is at maximum in the cores (Sps_{26}) and decreases continuously through the mantles to a minimum of Sps_{15} in the rims, typical of prograde growth. Almandine content increases continuously from Alm_{58} in the cores up to Alm_{69} in the rims. Both pyrope and grossular contents show a continuous zonation profile through the cores and mantles, with compositions of $Py_{7.5}Grs_6$ with X_{Mg} at 0.11 in the cores to $Py_{10}Grs_4$ and X_{Mg} at 0.13–0.14 in the mantles. Both of these components then show a sharp decrease or increase, respectively, in a thin, asymmetric rim, which can be observed most clearly in the Ca map. The composition of this rim is around $Alm_{69}Py_9Grs_6Sps_{15}$ with an X_{Mg} of 0.12–0.13. The Ca map also shows growth zoning between the cores and mantles, however the continuity from cores through mantles in the other maps indicates that some diffusion has likely contributed to smoothing the profiles. The thin rims are asymmetric with respect to the S_3 foliation, which indicates syn-S_3 growth of the rims. Garnet cores are therefore likely related to pre-S_3 metamorphism and rims related to shear zone deformation.

Based on the mineral textures and garnet zoning, two mineral assemblages can be defined for determination of a P-T path; a pre-S_3 assemblage includes garnet (cores) + ilmenite + quartz ±

andalusite ± staurolite, and a syn-S_3 assemblage of garnet (rims) + biotite + chlorite + muscovite + quartz + ilmenite.

P-T conditions and a P-T path were established for metamorphism of the schist mylonite (sample CS18-32) using phase equilibrium modeling with the following solution models: Gt(HP), Chl(HP), Mica(CHA1), Bio(TCC), feldspar, St(HP), Ctd(HP), IlGkPy, and Ep(HP) (Fuhrman & Lindsley, 1988; Holland & Powell, 1998; Tajčmanová et al., 2009; Auzanneau et al., 2010). The modeled sample contains no graphite, but apatite is present and therefore the corresponding amount of CaO bonded to P_2O_5 observed in the whole-rock analysis was subtracted from the bulk composition (Table S5). Since garnet cores (and mantles) and rims represent different metamorphic stages with respect to S_3, they were modeled in two separate P-T sections (Fig. 8). Note that these calculations have an uncertainty of ±50 °C (Powell & Holland, 2008; Palin et al., 2016). Garnet core and mantle P-T conditions were modeled in the system MnO-Na_2O-CaO-K_2O-FeO-MgO-Al_2O-SiO_2-TiO_2-H_2O with H_2O as a saturated phase (Fig. 8a). Measured garnet core compositions match modeled garnet compositions at the garnet-in line between 525–540 °C and 340–370 MPa within the stability field Grt-Bt-Ms-Chl-Pl-Ilm-Qz, which is consistent with the presence of ilmenite inclusions in garnet cores. The increase in X_{Mg} and almandine content and decrease in spessartine and grossular content from garnet cores through mantles indicates garnet growth during an increase in temperature to conditions of 550–565 °C and 340–370 MPa. Measured garnet mantle compositions match modeled garnet isopleths in and around phase fields that include both andalusite and staurolite, suggesting that these two minerals grew concurrent with garnet mantle growth primarily related to heating.

To account for fractionation, garnet rims were modeled separately using a bulk composition from which garnet cores and mantles were removed (Fig. 8b). Based on thin section observations and volume percentage predicted by the P-T section for garnet cores and mantles, 0.45 vol% garnet with a composition averaged from garnet cores and mantles ($Alm_{61}Sps_{22}Py_9Grs_5$) was subtracted from the whole rock composition. Minor magnetite present in the matrix indicates the presence of ferric iron, and it is also therefore appropriate to consider the redox budget in the calculation. O_2 content was estimated from a T-X_{O2} section at 400 MPa calculated for the new bulk composition (Fig. S4). The stability of magnetite and the garnet rim compositions suggest that

between 0.04 and 0.10 wt% O_2 may have been present in the system during shearing. We therefore added 0.07 wt% O_2 to the bulk composition to estimate P-T conditions of garnet rim growth and shearing.

The decrease in pyrope content and increase in grossular content in the garnet growth rims relative to the mantles indicates an increase in pressure during development of S_3, which destabilized andalusite and staurolite. The garnet rim compositions plot at the now higher-temperature garnet-in line (from fractionation), recording P-T conditions of 550–570 °C and 450–490 MPa with the following phases stable: Grt-Bt-Ms-Chl-Pl-Mag-Qz, which is consistent with the S_3 mineral assemblage (Fig. 8b). Matrix biotite compositions (X_{Mg} = 0.46–0.49) match corresponding isopleths that are mostly consistent with this garnet rim estimate, plotting at only slightly higher temperatures (570–590 °C). This estimate indicates the peak pressure recorded by garnet growth related to shearing deformation, although the presence of minor rutile in the sample suggests conditions may have reached higher pressures (above 700–900 MPa). However, the lack of evidence of equilibration in other minerals makes these conditions impossible to estimate, but the P-T modeling shows a clear pattern of an initial phase of heating, followed by a near-isothermal pressure increase.

Peak temperature estimates were also calculated from the Ti content of biotite following the method of Henry et al. (2005). Biotite grains selected for geothermometry were inclusion-free, showed no retrogression textures, and were not in contact with garnet. The Ti contents suggest peak metamorphic temperatures were primarily between 550–600 °C with an error of ±24 °C (Fig. 9; Table S6). This temperature estimate is consistent across the four samples from the LRS mylonite and matches the temperature range predicted by the phase equilibrium modeling.

The metabasalt mylonites contain a syn-kinematic mineral assemblage of amphibole + plagioclase + epidote + titanite ± chlorite ± quartz. Large amphibole porphyroblasts have chemically distinct cores and tails (Fig. 6b) and sometimes contain inclusions of titanite and plagioclase (Fig. 6c). Fine-grained amphibole, plagioclase, epidote, titanite, and ilmenite surround the amphibole porphyroblasts. Titanite and ilmenite occur as discontinuous seams often wrapping around amphibole grains with titanite sometimes enveloping large ilmenite grains.

Quartz and chlorite occur as minor phases, with quartz present as fine grains within the matrix and rare chlorite present along amphibole tails. Fine-grained layers of epidote and amphibole with interspersed ribbons of plagioclase may represent relict epidote veins (Fig. 6d).

P-T conditions during metamorphism of the metabasalt mylonite were constrained with amphibole and plagioclase compositions (Fig. 10; Table S7 and S8). Spot analyses and maps document increasing Fe, Al, Ti, and Na content and decreasing Mg and Si content from amphibole cores to rims/tails (Fig. 10a,c). The Si, Al, and Na distribution in amphibole structural sites depends on the pressure and temperature during growth (Ernst & Liu, 1998; Spear, 1981, 1995). Amphibole transitions from actinolite cores to hornblende/tschermakite rims via the pressure-sensitive Al-Tschermak substitution ($^{T}Si + {}^{M1\text{-}M3}Mg = {}^{T}Al + {}^{M1\text{-}M3}Al$). The positive correlation between A site occupancy and tetrahedrally-coordinated Al (Al^{iv}) records the temperature-sensitive edenite exchange ($^{T}Si + {}^{A}[\ ] = {}^{T}Al + {}^{A}(Na + K)$). Growth of magnesio-hornblende amphibole rims suggests peak metamorphic temperatures were >420 °C, providing a minimum constraint (Maruyama et al., 1983). Additionally, TiO_2 in amphibole increases from 0.05–0.15 in the cores to 0.20–0.50 in the rims. The increasing TiO_2 content is consistent with increasing temperature (Ernst & Liu, 1998). These trends record prograde amphibole growth during deformation. Metamorphic plagioclase compositions are oligoclase to andesine ($An_{26–45}$; Fig. 10b), which are typical of amphibolite facies metamorphism and the calcification of plagioclase, caused by increasing temperature, is consistent with the actinolite-to-hornblende transition (Maruyama et al., 1982; Maruyama et al., 1983; Spear, 1995).

6 Discussion

6.1 The Leech River Shear Zone: a paleo-subduction thrust

Our field and microstructural observations are the first to document reverse-sinistral displacement across the LRSZ and define the LRSZ as a high strain zone distinct from the surrounding rocks. The kinematic interpretation is based on the steeply plunging lineation, north-side-up reverse-sense kinematic indicators in sub-vertical exposures, and sinistral-sense indicators in sub-horizontal exposures. We interpret the thinner, more repetitive compositional layering, composite foliations, and finer grain size in the schist mylonite to be the result of higher shear strain accumulated during further isoclinal folding, layer thinning, and transposition

relative to the folding and disruption of bedding observed in the schist north of the LRSZ. The S_2 foliation in the Leech River Schist north of the mylonite zone is parallel to the mylonitic foliation (S_3) in both the schist and metabasalt mylonites, and the vergence direction throughout the schist and within the mylonite zone are similar, indicating that deformation of the entire package involved one predominant shortening direction with higher strain localized in the LRSZ. These interpretations are broadly consistent with previous observations (Fairchild & Cowan, 1982; Groome et al., 2003), though our results establish the importance of the reverse-sense motion across the LRSZ.

Metamorphic conditions in the schist and metabasalt mylonites in the LRSZ are consistent with deformation at amphibolite facies. In the schist mylonites, metamorphism involved an initial phase of heating at low pressure to amphibolite facies conditions, resulting in the pre-kinematic growth of biotite, staurolite, andalusite, and garnet (cores and mantles), followed by a sharp increase in pressure, resulting in the destabilization of staurolite and andalusite and syn-kinematic growth of muscovite, chlorite, biotite, and garnet (rims). This progression outlines a qualitative anticlockwise P-T path. Temperature and pressure estimates of 550–570 °C and 450–490 MPa from garnet rim compositions (Fig. 8) are further supported by peak temperature estimates of 550–575 °C from Ti-in-biotite geothermometry (Fig. 9). In the metabasalt mylonites, the transition from actinolite cores to hornblende rims in porphyroclasts indicates the transition from greenschist to amphibolite facies (Fig. 10). Similar P-T conditions during syn-kinematic mineral growth in both the schist and metabasalt mylonites demonstrate that strain caused by reverse-sense motion was distributed across both units at peak P-T.

The metamorphic mineralogy of the schist and metabasalt mylonites is consistent with previous observations of the Leech River Schist and Metchosin Basalt from outside the LRSZ (Fairchild & Cowan, 1982; Rusmore & Cowan, 1985; Groome et al., 2003; Timpa et al., 2005). However, previous P-T estimates for the Leech River Schist were restricted to high-temperature, low-pressure metamorphism based on the presence of andalusite (Fairchild & Cowan, 1982; Groome et al., 2003). Our observations show that andalusite in the schist mylonite is rare, small (<1 cm), and exhibits disequilibrium textures, with chlorite and muscovite replacing andalusite and forming syn-kinematic tails (e.g., Fig. 5e). We therefore interpret andalusite growth to pre-date

syn-kinematic metamorphism in the LRSZ, which is associated with a pressure increase of at least 100–200 MPa, or higher, based on the presence of rutile. This increase in burial depth after the high T, low P metamorphism suggests upper plate thickening associated with the underthrusting of the MIC occurred before and during the final docking of the MIC basalts in their current position relative to the structurally overlying LRC.

P-T estimates for the schist mylonites correspond to a geothermal gradient of ~30 °C/km when the LRSZ was active, which is higher than the hottest modern subduction zones (Penniston-Dorland et al., 2015; Syracuse et al., 2010). However, geothermal gradients as high as 50 °C/km during ridge subduction have been reported in other subduction complexes (e.g., Sisson et al., 1989; Pavlis & Sisson, 1995; Sakaguchi, 1996; Brown, 1998; Zumsteg et al., 2003). The elevated temperatures estimated from the LRSZ are likely due to the anomalously high geothermal gradients produced by subduction of the Kula/Resurrection-Farallon Ridge beneath the forearc, the young age of the subducting plate, and the nearby Yellowstone hotspot (Breitsprecher et al., 2003; Groome & Thorkelson, 2009).

The southward increase in metamorphic grade from greenschist to amphibolite facies in the LRS does not exhibit the inverted thermal gradient typical of subduction systems (Peacock, 1987). We suggest that the regional thermal structure of the LRC was established by heating from below by a young, hot, plume-affected oceanic plate, rather than refrigeration by a cold slab. Throughout the LRC, isoclinal, asymmetric folds with top-to-the-south vergence appear to have developed either prior to and/or at the local peak conditions, representing regional shortening during burial. The consistency of the attitudes of the S_2 regional foliation with the S_3 mylonitic foliation suggests this shortening could have occurred within the upper plate during convergence. Throughout the LRC, isoclinal, asymmetric folds with top-to-the-south vergence are consistent with shortening of the upper plate during convergence. The late near-isothermal increase in pressure recorded by the mylonites was likely due to tectonic burial by wedge shortening and thickening during underthrusting as strain localized onto the LRSZ. This interpretation implies the noncoaxial deformation in the LRSZ during the syn-kinematic growth of garnet rims only records the latest phase in the subduction history of the MIC as it progressed from the trench to peak P-T conditions.

Overall, the shear zone kinematics and anticlockwise P-T path with heating followed by a pressure increase, combined with the juxtaposition of a fragment of oceanic crust against an underplated terrigenous complex, all suggest that the LRSZ is a sinistral-oblique thrust that accommodated underthrusting of the Siletz-Crescent terrane beneath the North American margin in a subduction zone setting. The kinematics and syn-kinematic prograde metamorphic conditions inferred in both lithologies within the LRSZ are inconsistent with alternative hypotheses for the LRSZ tectonic setting (i.e., dominantly strike-slip motion (e.g., Fairchild & Cowan, 1982) or development as part of a forearc rift (e.g., Babcock et al., 1992)). Although the thermal history of the LRSZ is atypical of subduction assemblages, we conclude that the LRSZ represents a hot paleo-subduction interface.

6.2 Tectonic history of the Leech River Complex and Leech River Shear Zone

The LRSZ forms the tectonic contact between the LRC and MIC of the Siletz-Crescent terrane and therefore its deformation history can be used to inform the tectonic history of the surrounding units. Our results provide new constraints on the origin of the LRC. Detrital zircon U-Pb ages indicate an early Paleocene MDA for the Leech River Schist and Jordan River Unit of the LRC, which is significantly younger than previously reported Late Jurassic to Cretaceous deposition estimates based on whole-rock Rb-Sr isotopic data (Fairchild & Cowan, 1982) and youngest zircon U-Pb ages (Groome et al., 2003). These new ages for the LRC place an upper bound on when the LRSZ was active, and they are broadly consistent with underthrusting of the MIC in the Eocene (Eddy et al., 2017).

Detrital zircon age distributions from the LRC provide further constraints on its depositional context and further tests whether the LRC is an allochthonous terrane. The LRC has a similar age distribution to two groups of sedimentary rocks: the youngest (Maastrichtian- to early Paleocene-age) formations in the Upper Nanaimo Group on Vancouver Island (Coutts et al., 2020; Englert et al., 2018; Matthews et al., 2017) and the Yakutat Group in Alaska, which has previously been correlated with the Pacific Rim terrane (Garver & Davidson, 2015). The Upper Nanaimo Group was deposited in a marine subduction forearc basin (Coutts et al., 2020). The Yakutat Group, part of the Chugach-Prince William terrane, was deposited as trench-fill turbidites, then

632 incorporated into an accretionary complex (Garver & Davidson, 2015). The LRC shares similar
633 MDA, peaks in Proterozoic ages at 1850–1560 Ma and 1450–1300 Ma, and absence of grains
634 with 1000–1300 Ma ages with these units (Fig. 3b). For both the Upper Nanaimo Group and
635 Yakutat Group, previous work interpreted detrital zircon grains with Mesozoic and early
636 Paleocene ages (200–60 Ma) to be derived from the Coast Mountains Batholith, while
637 Proterozoic (1850–1560 and 1450–1300 Ma) zircons were interpreted to be sourced from the
638 Yavapai and Mazatzal terranes of southwestern Laurentia (Coutts et al., 2020; Dumitru et al.,
639 2016; Garver & Davidson, 2015; Housen & Beck, 1999; Matthews et al., 2017). It is important
640 to note that the source of these Proterozoic-age zircons and the paleolatitude of the Nanaimo
641 Group is an ongoing debate. However, we suggest these interpretations of detrital zircon source
642 regions are also applicable to the LRC.
643
644 The LRC was previously interpreted as allochthonous to Vancouver Island (Fairchild & Cowan,
645 1982), but these new detrital zircon ages support an alternative interpretation. We suggest the
646 similar detrital zircon age distributions (and therefore similar sources) of the LRC and Upper
647 Nanaimo Group as demonstrate that these units were derived from similar sedimentary sources,
648 and therefore likely deposited near each other in the latest Cretaceous to early Paleocene. This
649 model also implies that the LRC was deposited in proximity to the Wrangellia terrane, which
650 constitutes the majority of Vancouver Island, as the Nanaimo Group uncomfortably overlies the
651 Wrangellia terrane (Mustard, 1994). Our data do not directly test whether there has been any
652 relative motion between the LRC and Wrangellia; however, the simplest explanation for the
653 similarity between the LRC and Nanaimo Group ages is that the LRC represents a marine
654 sequence that shared the same source region at the same time as the Nanaimo Group basin. This
655 tectonic context, the mixed lithologies of the LRC (psammitic, pelitic, and mafic volcanics), and
656 the similar depositional age of the Upper Nanaimo suggest the LRC represents an assemblage of
657 metamorphosed marine basin rocks, likely deposited in a near-margin trench environment.
658 Within the LRC, the structural record of block-in-matrix textures, transposition of bedding, and
659 layer-perpendicular veins, which are typical of underthrust subduction complexes (e.g.,
660 Connelly, 1978; Fisher & Byrne, 1987; Pavlis & Sisson, 1995; Meneghini et al., 2009; Ujiie,
661 2002). Furthermore, the LRS depositional age is broadly correlative with the Chugach
662 accretionary complex, and possibly parts of the Franciscan complex, which together record

subduction off the west coast of North America in the latest Cretaceous and Paleocene (Cowan, 1982, 2003; Garver & Davidson, 2015). We therefore conclude that the LRC is not as an allochthonous terrane, but represents an accretionary complex developed from trench-fill sediments consistent with the North American margin.

We summarize our results with available timing constraints on the tectonic history of the LRC, Siletz-Crescent, and LRSZ from the literature (Fig. 11). At ~65–60 Ma (Fig. 11a), the Leech River Schist (MDA ~66–61 Ma) and Upper Nanaimo Group (MDA ~80–64 Ma) were deposited in near-margin trench and forearc basins, respectively, with the Nanaimo Group unconformably overlying the Wrangellia terrane (this study; Coutts et al., 2020; Englert et al., 2018; Matthews et al., 2017). Any northward coast-wise transport of all three units occurred during oblique subduction (Coutts et al., 2020; Matthews et al., 2017). At ~52 Ma (Fig. 11b), the Metchosin Basalt was erupted as part of an oceanic plateau (U-Pb zircon age of 52±2 Ma; Massey, 1986), while the LRC was underthrust and deformed as an accretionary complex during subduction of the Kula/Resurrection and Farallon plates, and the Nanaimo Group was shallowly buried (Stewart & Page, 1974). The Kula/Resurrection-Farallon ridge (and slab window) was subducted ahead of the Metchosin Basalt. By ~51–48 Ma (Fig. 11c), during the accretion of the Siletz-Crescent terrane to the North American margin (Eddy et al., 2017), the Metchosin Basalt was subducted beneath the Leech River Schist along the LRSZ, and the Cowichan fold-and-thrust belt developed in the Nanaimo Group (England & Calon, 1991). Shortening and thickening of the upper plate buried the active LRSZ, causing a near-isothermal pressure increase during shear. Shortly thereafter, the Metchosin Basalt, and the LRSZ itself, were underplated and accreted to the overriding continent as the décollement stepped further west. Emplacement of the Walker Creek intrusions pin the location of the schist to its current latitude from ~51 Ma to the present (Breitsprecher et al., 2003; Groome et al., 2003). Additionally, some of these intrusions exhibit deformation while others are not deformed (Groome et al., 2003), indicating syn- to post-kinematic emplacement and marking the cessation of deformation in the LRSZ and underplating of the Metchosin Basalt. Following underplating, the LRC was exhumed through the mica cooling temperatures ($^{40}Ar/^{39}Ar$ ages of 45.2±0.2 Ma and 42.5±0.2 Ma in muscovite and biotite, respectively; Groome et al., 2003). Exhumation may have been accommodated by a structurally lower fault during subsequent subduction (e.g. at the base of the MIC), though this is currently

untested. Unconformable deposition of the coastal marine Carmanah Group across the LRSZ in the Oligocene constrains the exposure of the units at the surface (Fig. 11d; Harrichhausen, 2021; Muller, 1977a). The compatibility of this re-interpretation with previous work on the tectonic history and timing of accretion of the Siletz-Crescent terrane (Eddy et al., 2016; Groome et al., 2003; McCrory & Wilson, 2013; Wells et al., 2014), reinforces the interpretation that the LRSZ was a hot subduction plate boundary interface in the Eocene.

7 Conclusions

This study evaluates the LRSZ as a possible paleo-subduction interface. Structural, kinematic, and petrologic evidence from the LRSZ indicates hot rocks underwent reverse-sinistral sense deformation during a near-isothermal pressure increase at amphibolite facies conditions related to underthrusting during subduction. The elevated geothermal gradient implied by the P-T conditions likely resulted from subduction of the Kula/Resurrection-Farallon Ridge, subsequent formation of a slab window, and the nearby Yellowstone Hotspot. These observations are consistent with tectonic models of the hotspot location and plate motions during the Eocene (~50 Ma). Detrital zircon age distributions suggest the Leech River Schist is a Paleocene-age accretionary complex that was deposited in proximity to the Upper Nanaimo Group and Wrangellia terrane, and therefore the LRC is not allochthonous to Vancouver Island. Overall, we establish that the LRSZ represents a paleo-subduction interface from an anomalously hot Eocene subduction zone.

Acknowledgements

We thank TimberWest and Hydro BC for assistance in accessing the field area. C.S. acknowledges support from the Fonds de recherche du Québec – Nature et technologies (FRQNT). J.K. acknowledges support from the Natural Sciences and Engineering Research Council of Canada (NSERC), Discovery Grant RGPIN-2022-04193. D.S. acknowledges support from an NSERC Undergraduate Student Research Award (USRA). A.L. acknowledges support from the University of Washington and thanks Tamas Ugrai and Samuel Shekut for assistance in the lab. C.R. acknowledges support from NSF EAR IRFP Grant #1349586 and NSF EAR Tectonics Grant #1756834. Thanks to Sarah Roeske and an anonymous reviewer for constructive reviews that greatly improved the manuscript.

Open Research

The whole rock compositional data, mineral composition data, detrital zircon U-Pb analyses, and structural data are available in the supplementary information. The geochemical data (whole rock, mineral, and detrital zircon U-Pb) are also available through the EarthChem (https://doi.org/10.26022/IEDA/112312). *PerpleX* version 6.9.9 (Connolly, 2005) was used for phase equilibrium modeling and is developed openly at https://www.perplex.ethz.ch/.

References

Auzanneau, E., Schmidt, M. W., Vielzeuf, D., & Connolly, J. A. D. (2010). Titanium in phengite: a geobarometer for high temperature eclogites. *Contributions to Mineralogy and Petrology, 159*(1), 1. https://doi.org/10.1007/s00410-009-0412-7

Babcock, R. S., Burmester, R. F., Engebretson, D. C., Warnock, A., & Clark, K. P. (1992). A rifted margin origin for the crescent basalts and related rocks in the northern Coast Range Volcanic Province, Washington and British Columbia. *Journal of Geophysical Research: Solid Earth, 97*(B5), 6799-6821. https://doi.org/10.1029/91JB02926

Behr, W. M., Holt, A. F., Becker, T. W., & Faccenna, C. (2022). The effects of plate interface rheology on subduction kinematics and dynamics. *Geophysical Journal International, 230*(2), 796-812. https://doi.org/10.1093/gji/ggac075

Breitsprecher, K., Thorkelson, D. J., Groome, W. G., & Dostal, J. (2003). Geochemical confirmation of the Kula-Farallon slab window beneath the Pacific Northwest in Eocene time. *Geology, 31*(4), 351-354. https://doi.org/10.1130/0091-7613(2003)031<0351:GCOTKF>2.0.CO;2

Brown, M. (1998). Ridge–trench interactions and high-T–low-P metamorphism, with particular reference to the Cretaceous evolution of the Japanese Islands. *Geological Society, London, Special Publications, 138*, 137-169. https://doi.org/10.1144/GSL.SP.1996.138.01.09

Cecil, M. R., Rusmore, M. E., Gehrels, G., Woodsworth, G., Stowell, H. H., Yokelson, I. N., et al. (2018). Along-strike variation in the magmatic tempo of the Coast Mountains Batholith, British Columbia, and implications for processes controlling episodicity in arcs. *Geochemistry, Geophysics, Geosystems, 19*(11), 4274-4289. https://doi.org/10.1029/2018GC007874

753 Chelle-Michou, C., McCarthy, A., Moyen, J.-F., Cawood, P. A., & Capitanio, F. A. (2022).
754 Make subductions diverse again. *Earth-Science Reviews, 226,* 103966.
755 https://doi.org/10.1016/j.earscirev.2022.103966
756 Clowes, R. M., Brandon, M. T., Green, A. G., Yorath, C. J., Brown, A. S., Kanasewich, E. R., &
757 Spencer, C. (1987). LITHOPROBE--southern Vancouver Island: Cenozoic subduction
758 complex imaged by deep seismic reflections. *Canadian Journal of Earth Sciences, 24*(1),
759 31-51. https://doi.org/10.1139/e87-004
760 Connelly, W. (1978). Uyak Complex, Kodiak Islands, Alaska: A Cretaceous subduction
761 complex. *Geological Society of America Bulletin, 89*(5), 755-769.
762 https://doi.org/10.1130/0016-7606(1978)89<755:UCKIAA>2.0.CO;2
763 Connolly, J. A. D. (2005). Computation of phase equilibria by linear programming: a tool for
764 geodynamic modeling and its application to subduction zone decarbonation. *Earth and*
765 *Planetary Science Letters, 236*, 524-541. https://doi.org/10.1016/j.epsl.2005.04.033
766 Coutts, D., Matthews, W. A., Englert, R. G., Brooks, M. D., Boivin, M.-P., & Hubbard, S.
767 (2020). Along-strike variations in sediment provenance within the Nanaimo basin reveal
768 mechanisms of forearc basin sediment influx events. *Lithosphere, 12*(1), 180-197.
769 https://doi.org/10.1130/L1138.1
770 Cowan, D. S. (1982). Geological evidence for post-40 m.y. B.P. large-scale northwestward
771 displacement of part of southeastern Alaska. *Geology, 10*, 309-313.
772 https://doi.org/10.1130/0091-7613(1982)10<309:GEFPMB>2.0.CO;2
773 Cowan, D. S. (2003). Revisiting the Baranof-Leech River hypothesis for early Tertiary coastwise
774 transport of the Chugach-Prince William terrane. *Earth and Planetary Science Letters,*
775 *213*(3-4), 463-475. https://doi.org/10.1016/S0012-821X(03)00300-5
776 Cowan, D. S., Brandon, M. T., & Garver, J. I. (1997). Geologic tests of hypotheses for large
777 coastwise displacements—A critique illustrated by the Baja British Columbia
778 controversy. *American Journal of Science, 297*(2), 117-173.
779 https://doi.org/10.2475/ajs.297.2.117
780 Cui, Y., Miller, D., Schiarizza, P., & Diakow, L. J. (2017). *British Columbia digital geology*.
781 British Columbia Ministry of Energy, Mines and Petroleum Resources, British Columbia
782 Geological Survey Open File 2017-8, Data version 2019-12-19.

DeLong, S. E., Schwarz, W. M., & Anderson, R. N. (1979). Thermal effects of ridge subduction. *Earth and Planetary Science Letters, 44*, 239-246. https://doi.org/10.1016/0012-821X(79)90172-9

Dumitru, T. A., Elder, W. P., Hourigan, J. K., Chapman, A. D., Graham, S. A., & Wakabayashi, J. (2016). Four Cordilleran paleorivers that connected Sevier thrust zones in Idaho to depocenters in California, Washington, Wyoming, and, indirectly, Alaska. *Geology, 44*(1), 75-78. https://doi.org/10.1130/G37286.1

Duncan, R. A. (1982). A captured island chain in the Coast Range of Oregon and Washington. *Journal of Geophysical Research: Solid Earth, 87*(B13), 10827-10837. https://doi.org/10.1029/JB087iB13p10827

Eddy, M. P., Bowring, S. A., Umhoefer, P. J., Miller, R. B., McLean, N. M., & Donaghy, E. E. (2016). High-resolution temporal and stratigraphic record of Siletzia's accretion and triple junction migration from nonmarine sedimentary basins in central and western Washington. *Geological Society of America Bulletin, 128*(3-4), 425-441. https://doi.org/10.1130/B31335.1

Eddy, M. P., Clark, K. P., & Polenz, M. (2017). Age and volcanic stratigraphy of the Eocene Siletzia oceanic plateau in Washington and on Vancouver Island. *Lithosphere, 9*(4), 652-664. https://doi.org/10.1130/L650.1

England, T. D. J., & Calon, T. J. (1991). The Cowichan fold and thrust system, Vancouver Island, southwestern British Columbia. *Geological Society of America Bulletin, 103*, 336-362. https://doi.org/10.1130/0016-7606(1991)103<0336:TCFATS>2.3.CO;2

Englert, R. G., Hubbard, S., Coutts, D., & Matthews, W. A. (2018). Tectonically controlled initiation of contemporaneous deep- water channel systems along a Late Cretaceous continental margin, western British Columbia, Canada. *Sedimentology, 65*, 2404-2438. https://doi.org/10.1111/sed.12472

Ernst, W. G., & Liu, J. (1998). Experimental phase-equilibrium study of Al- and Ti-contents of calcic amphibole in MORB—A semiquantitative thermobarometer. *American Mineralogist, 83*, 952-969. https://doi.org/10.2138/am-1998-9-1004

Evans, T. P. (2004). A method for calculating effective bulk composition modification due to crystal fractionation in garnet-bearing schist: implications for isopleth thermobarometry.

Journal of Metamorphic Geology, 22(6), 547-557. https://doi.org/10.1111/j.1525-1314.2004.00532.x

Fairchild, L. H., & Cowan, D. S. (1982). Structure, petrology, and tectonic history of the Leech River complex northwest of Victoria, Vancouver Island. *Canadian Journal of Earth Sciences, 19*(9), 1817-1835. https://doi.org/10.1139/e82-161

Fisher, D., & Byrne, T. (1987). Structural evolution of underthrusted sediments, Kodiak Islands, Alaska. *Tectonics, 6*(6), 775-793. https://doi.org/10.1029/TC006i006p00775

Friedman, R. M., & Armstrong, R. L. (1995). Jurassic and Cretaceous geochronology of the southern Coast Belt, British Columbia, 49° to 51°N. *Special Papers-Geological Society of America, 299*, 95-139. https://doi.org/10.1130/SPE299-p95

Fuhrman, M. L., & Lindsley, D. H. (1988). Ternary-feldspar modeling and thermometry. *American Mineralogist, 73*(3-4), 201-215.

Garver, J. I., & Davidson, C. M. (2015). Southwestern Laurentian zircons in Upper Cretaceous flysch of the Chugach-Prince William terrane in Alaska. *American Journal of Science, 315*(6), 537-556. https://doi.org/10.2475/06.2015.02

Gehrels, G., Rusmore, M. E., Woodsworth, G., Crawford, M., Andronicos, C., Hollister, L., et al. (2009). U-Th-Pb geochronology of the Coast Mountains batholith in north-coastal British Columbia: Constraints on age and tectonic evolution. *Geological Society of America Bulletin, 121*(9-10), 1341-1361. https://doi.org/10.1130/B26404.1

Groome, W. G. (2000). *Magmatism and Metamorphism in the Leech River Complex, Southern Vancouver Island, British Columbia, Canada: Implications for Eocene Tectonics of the Pacific Northwest* (Master's thesis). Vancouver, BC: Simon Fraser University.

Groome, W. G., & Thorkelson, D. J. (2009). The three-dimensional thermo-mechanical signature of ridge subduction and slab window migration. *Tectonophysics, 464*, 70-83. https://doi.org/10.1016/j.tecto.2008.07.003

Groome, W. G., Thorkelson, D. J., Friedman, R. M., Mortensen, J. K., Massey, N. W. D., Marshall, D. D., & Layer, P. W. (2003). Magmatic and tectonic history of the Leech River Complex, Vancouver Island, British Columbia: Evidence for ridge-trench intersection and accretion of the Crescent Terrane. *Special Papers-Geological Society of America, 371*, 327-353. https://doi.org/10.1130/0-8137-2371-X.327

Harrichhausen, N. (2021). *Fault accommodation of permanent strain in the northern Cascadia forearc* (Doctoral thesis). (https://escholarship.org/uc/item/5h05p9fv). Santa Barbara, CA: University of California, Santa Barbara.

Harrichhausen, N., Morell, K. D., Regalla, C., Bennett, S. E., Leonard, L. J., Lynch, E. M., & Nissen, E. (2021). Paleoseismic trenching reveals Late Quaternary kinematics of the Leech River Fault: Implications for forearc strain accumulation in northern Cascadia *Bulletin of the Seismological Society of America, 111*(2), 1110-1138. https://doi.org/10.1785/0120200204

Hawthorne, F. C., Oberti, R., Harlow, G. E., Maresch, W. V., Martin, R. F., Schumacher, J. C., & Welch, M. D. (2012). Nomenclature of the amphibole supergroup. *American Mineralogist, 97*, 2031-2048. http://doi.org/10.2138/am.2012.4276

Henry, D. J., Guidotti, C. V., & Thomson, J. A. (2005). The Ti-saturation surface for low-to-medium pressure metapelitic biotites: Implications for geothermometry and Ti-substitution mechanisms. *American Mineralogist, 90*(2-3), 316-328. https://doi.org/10.2138/am.2005.1498

Holland, T. J. B., & Powell, R. (1998). An internally consistent thermodynamic data set for phases of petrological interest. *Journal of Metamorphic Geology, 16*(3), 309-343. https://doi.org/10.1111/j.1525-1314.1998.00140.x

Holt, A. F., & Condit, C. B. (2021). Slab temperature evolution over the lifetime of a subduction zone. *Geochemistry, Geophysics, Geosystems, 22*(6), e2020GC009476. https://doi.org/10.1029/2020GC009476

Horstwood, M. S. A., Košler, J., Gehrels, G., Jackson, S. E., McLean, N. M., Paton, C., et al. (2016). Community- Derived Standards for LA- ICP- MS U- (Th-)Pb Geochronology – Uncertainty Propagation, Age Interpretation and Data Reporting. *Geostandards and Geoanalytical Research, 40*(3), 311-332. https://doi.org/10.1111/j.1751-908X.2016.00379.x

Housen, B., & Beck, M. E. (1999). Testing terrane transport: An inclusive approach to the Baja B.C. controversy. *Geology, 27*(12), 1143-1146. https://doi.org/10.1130/0091-7613(1999)027<1143:TTTAIA>2.3.CO;2

872 Hyndman, R. D., Yorath, C. J., Clowes, R. M., & Davis, E. E. (1990). The northern Cascadia
873 subduction zone at Vancouver Island: seismic structure and tectonic history. *Canadian*
874 *Journal of Earth Sciences, 27*(3), 313-329. https://doi.org/10.1139/e90-030
875 Irving, E. (1979). Paleopoles and paleolatitudes of North America and speculations about
876 displaced terrains. *Canadian Journal of Earth Sciences, 16*(3), 669-694.
877 https://doi.org/10.1139/e79-065
878 Leake, B. E., Woolley, A. R., Arps, C. E. S., Birch, W. D., Gilbert, M. C., Grice, J. D., et al.
879 (1997). Nomenclature of amphiboles: Report of the subcommittee on amphiboles of the
880 International Mineralogical Association, Commission on new minerals and mineral
881 names. *Mineralogical Magazine, 61*(405), 295-310.
882 https://doi.org/10.1180/minmag.1997.061.405.13
883 Li, G., Liu, Y., Regalla, C., & Morell, K. D. (2018). Seismicity relocation and fault structure
884 near the Leech River Fault Zone, southern Vancouver Island. *Journal of Geophysical*
885 *Research: Solid Earth, 123,* 2841-2855. https://doi.org/10.1002/2017JB015021
886 Locock, A. J. (2014). An Excel spreadsheet to classify chemical analyses of amphiboles
887 following the IMA 2012 recommendations. *Computers & Geosciences, 62*, 1-11.
888 https://doi.org/10.1016/j.cageo.2013.09.011
889 Ludwig, K. R. (2003). User's manual for Isoplot 3.00, a geochronological toolkit for Microsoft
890 Excel. *4*, 25-32.
891 Maruyama, S., Liou, J. G., & Suzuki, O. (1982). The peristerite gap in low-grade metamorphic
892 rocks. *Contributions to Mineralogy and Petrology, 81*, 268-276.
893 https://doi.org/10.1007/BF00371681
894 Maruyama, S., Suzuki, K., & Liou, J. G. (1983). Greenschist-amphibolite transition equilibria at
895 low pressures. *Journal of Petrology, 24*(4), 583-604.
896 https://doi.org/10.1093/petrology/24.4.583
897 Massey, N. W. D. (1986). Metchosin Igneous Complex, southern Vancouver Island: Ophiolite
898 stratigraphy developed in an emergent island setting. *Geology, 14*(7), 602-605.
899 https://doi.org/10.1130/0091-7613(1986)14%3C602:MICSVI%3E2.0.CO;2
900 Matharu, G., Bostock, M. G., Christensen, N. I., & Tromp, J. (2014). Crustal anisotropy in a
901 subduction zone forearc:Northern Cascadia. *Journal of Geophysical Research: Solid*
902 *Earth, 119,* 7058-7078. https://doi.org/10.1002/2014JB011321

Matthews, W. A., & Guest, B. (2017). A Practical Approach for Collecting Large- n Detrital Zircon U- Pb Data sets by Quadrupole LA- ICP- MS. *Geostandards and Geoanalytical Research, 41*(2), 161-180. https://doi.org/10.1111/ggr.12146

Matthews, W. A., Guest, B., Coutts, D., Bain, H., & Hubbard, S. (2017). Detrital zircons from the Nanaimo basin, Vancouver Island, British Columbia: An independent test of Late Cretaceous to Cenozoic northward translation. *Tectonics, 36*(5), 854-876. https://doi.org/10.1002/2017TC004531

McCrory, P. A., & Wilson, D. S. (2013). A kinematic model for the formation of the Siletz-Crescent forearc terrane by capture of coherent fragments of the Farallon and Resurrection plates. *Tectonics, 32*(3), 718-736. https://doi.org/10.1002/tect.20045

Meneghini, F., Marroni, M., Moore, J. C., Pandolfi, L., & Rowe, C. D. (2009). The processes of underthrusting and underplating in the geologic record: structural diversity between the Franciscan Complex (California), the Kodiak Complex (Alaska) and the Internal Ligurian Units (Italy). *Geological Journal, 44*(2), 126-152. http://doi.org/10.1002/gj.1144

Morell, K. D., Regalla, C., Amos, C., Bennett, S. E., Leonard, L. J., Graham, A., et al. (2018). Holocene surface rupture history of an active forearc fault redefines seismic hazard in southwestern British Columbia, Canada. *Geophysical Research Letters, 45*, 11605-11611. https://doi.org/10.1029/2018GL078711

Morell, K. D., Regalla, C., Leonard, L. J., Amos, C., & Levson, V. (2017). Quaternary rupture of a Crustal Fault beneath Victoria, British Columbia, Canada. *GSA Today, 27*(3), 4-10. https://doi.org/10.1130/GSATG291A.1

Muller, J. E. (1977a). Evolution of the Pacific Margin, Vancouver Island, and adjacent regions. *Canadian Journal of Earth Sciences, 14*(9), 2062-2085. http://doi.org/10.1139/e77-176

Muller, J. E. (1977b). Geology of Vancouver Island, British Columbia. *Geological Survey of Canada, Open File 463*. https://doi.org/10.4095/129265

Muller, J. E. (1980). Geology, Victoria, British Columbia. *Geological Survey of Canada, Open File 701*. https://doi.org/10.4095/129114

Mustard, P. S. (1994). The Upper Cretaceous Nanaimo Group, Georgia Basin. In J. Monger (Ed.), Geology and geological hazards of the Vancouver region, southwestern British Columbia (pp. 320). Geological Survey of Canada Bulletin 481. Retrieved from https://doi.org/10.4095/203244. doi:10.4095/203244

Nelson, J., & Colpron, M. (2007). Tectonics and metallogeny of the British Columbia, Yukon, and Alaskan Cordillera, 1.8 Ga to the present. In W. D. Goodfellow (Ed.), *Mineral Deposits of Canada: A Synthesis of Major Deposit-Types, District Metallogeny, the Evolution of Geological Provinces, and Exploration Methods* (pp. 755-791). St. John's, NL: Geological Association of Canada, Mineral Deposits Division, Special Publication No. 5.

Palin, R. M., Weller, O. M., Waters, D. J., & Dyck, B. (2016). Quantifying geological uncertainty in metamorphic phase equilibria modelling; a Monte Carlo assessment and implications for tectonic interpretations. *Geoscience Frontiers, 7*, 591-607. https://doi.org/10.1016/j.gsf.2015.08.005

Paton, C., Woodhead, J. D., Hellstrom, J. C., Hergt, J. M., Greig, A., & Maas, R. (2010). Improved laser ablation U- Pb zircon geochronology through robust downhole fractionation correction. *Geochemistry, Geophysics, Geosystems, 11*(3). https://doi.org/10.1029/2009GC002618

Pavlis, T. L., & Sisson, V. B. (1995). Structural history of the Chugach metamorphic complex in the Tana River region, eastern Alaska: A record of Eocene ridge subduction. *Geological Society of America Bulletin, 107*(11), 1333-1355. https://doi.org/10.1130/0016-7606(1995)107%3C1333:SHOTCM%3E2.3.CO;2

Peacock, S. M. (1987). Creation and preservation of subduction-related inverted metamorphic gradients. *Journal of Geophysical Research: Solid Earth, 92*(B12), 12763-12781. https://doi.org/10.1029/JB092iB12p12763

Penniston-Dorland, S. C., Kohn, M. J., & Manning, C. E. (2015). The global range of subduction zone thermal structures from exhumed blueschists and eclogites: Rocks are hotter than models. *Earth and Planetary Science Letters, 428*, 243-254. http://doi.org/10.1016/j.epsl.2015.07.031

Phillips, B. A., Kerr, A. C., Mullen, E. K., & Weis, D. (2017). Oceanic mafic magmatism in the Siletz terrane, NW North America: Fragments of an Eocene oceanic plateau? *Lithos, 274-275*, 291-303. https://doi.org/10.1016/j.lithos.2017.01.005

Powell, R., & Holland, T. J. B. (2008). On thermobarometry. *Journal of Metamorphic Geology, 26*, 155-179. https://doi.org /10.1111/j.1525-1314.2007.00756.x

964 Rusmore, M. E. (1982). *Structure and petrology of pre-tertiary rocks near Port Renfrew,*
965 *Vancouver Island, British Columbia* (Master's thesis). Seattle, WA: University of
966 Washington.
967 Rusmore, M. E., & Cowan, D. S. (1985). Jurassic–Cretaceous rock units along the southern edge
968 of the Wrangellia terrane on Vancouver Island. *Canadian Journal of Earth Sciences,*
969 *22*(8), 1223-1232. https://doi.org/10.1139/e85-124
970 Sakaguchi, A. (1996). High paleogeothermal gradient with ridge subduction beneath the
971 Cretaceous Shimanto accretionary prism, southwest Japan. *Geology, 24*(9), 795-798.
972 https://doi.org/10.1130/0091-7613(1996)024%3C0795:HPGWRS%3E2.3.CO;2
973 Seyler, C. E., Kirkpatrick, J. D., Faber, C., Licht, A., Šilerová, D., Regalla, C. (2022). Major
974 element whole rock and mineral analyses and U-Pb detrital zircon analyses of schist and
975 metabasalt mylonites from the Leech River Shear Zone, Version 1.0. Interdisciplinary
976 Earth Data Alliance (IEDA). https://doi.org/10.26022/IEDA/112312
977 Shekut, S., & Licht, A. (2020). Late Middle Miocene Emergence of the Olympic Peninsula
978 Shown by Sedimentary Provenance. *Lithosphere,* 1-20.
979 https://doi.org/10.2113/2020/7040598
980 Simpson, R. W., & Cox, A. (1977). Paleomagnetic evidence for tectonic rotation of the Oregon
981 Coast Range. *Geology, 5*(10), 585-589. https://doi.org/10.1130/0091-
982 7613(1977)5<585:PEFTRO>2.0.CO;2
983 Sisson, V. B., Hollister, L. S., Onstott, T. C. (1989). Petrologic and age constraints on the origin
984 of a low-pressure/high-temperature metamorphic complex, southern Alaska. *Journal of*
985 *Geophysical Research: Solid Earth, 94*(B4), 4392-4410.
986 https://doi.org/10.1029/JB094iB04p04392
987 Sláma, J., Košler, J., Condon, D. J., Crowley, J. L., Gerdes, A., Hanchar, J. M., et al. (2008).
988 Plešovice zircon — A new natural reference material for U-Pb and Hf isotopic
989 microanalysis. *Chemical Geology, 249*(1-2), 1-35.
990 https://doi.org/10.1016/j.chemgeo.2007.11.005
991 Spear, F. S. (1981). An experimental study of hornblende stability and compositional variability
992 in amphibolite. *American Journal of Science, 281*(6), 697-734.
993 https://doi.org/10.2475/ajs.281.6.697

Spear, F. S. (1995). *Metamorphic Phase Equilibria and Pressure-Temperature-Time-Paths* (2nd ed.). Washington, D.C.: Mineralogical Society of America.

Stewart, R. J., & Page, R. J. (1974). Zeolite Facies Metamorphism of the Late Cretaceous Nanaimo Group, Vancouver Island and Gulf Islands, British Columbia. *Canadian Journal of Earth Sciences, 11*, 280-284. https://doi.org/10.1139/e74-024

Syracuse, E. M., van Keken, P. E., & Abers, G. A. (2010). The global range of subduction zone thermal models. *Physics of the Earth and Planetary Interiors, 183*(1-2), 73-90. https://doi.org/10.1016/j.pepi.2010.02.004

Tajčmanová, L., Connolly, J. A. D., & Cesare, B. (2009). A thermodynamic model for titanium and ferric iron solution in biotite. *Journal of Metamorphic Geology, 27*(2), 153-165. https://doi.org/10.1111/j.1525-1314.2009.00812.x

Timpa, S., Gillis, K. M., & Canil, D. (2005). Accretion-related metamorphism of the Metchosin Igneous Complex, southern Vancouver Island, British Columbia. *Canadian Journal of Earth Sciences, 42*(8), 1467-1479. https://doi.org/10.1139/e05-043

Tréhu, A. M., Asudeh, I., Brocher, T. M., Luetgert, J. H., Mooney, W. D., Nabelek, J. L., & Nakamura, Y. (1994). Crustal architecture of the Cascadia forearc. *Science, 266*(5183), 237-243. https://doi.org/10.1126/science.266.5183.237

Ujiie, K. (2002). Evolution and kinematics of an ancient décollement zone, mélange in the Shimanto accretionary complex of Okinawa Island, Ryukyu Arc. *Journal of Structural Geology, 24*(5), 937-952. https://doi.org/10.1016/S0191-8141(01)00103-1

Wells, R., Bukry, D., Friedman, R., Pyle, D., Duncan, R., Haeussler, P., & Wooden, J. (2014). Geologic history of Siletzia, a large igneous province in the Oregon and Washington Coast Range: Correlation to the geomagnetic polarity time scale and implications for a long-lived Yellowstone hotspot. *Geosphere, 10*(4), 692-719. https://doi.org/10.1130/GES01018.1

Wells, R., Engebretson, D. C., Snavely Jr., P. D., & Coe, R. S. (1984). Cenozoic plate motions and the volcano- tectonic evolution of western Oregon and Washington. *Tectonics, 3*(2), 275-294. https://doi.org/10.1029/TC003i002p00275

White, R. W., Powell, R., Holland, T., & Worley, B. (2000). The effect of TiO2 and Fe2O3 on metapelitic assemblages at greenschist and amphibolite facies conditions: mineral equilibria calculations in the system K2O-FeO-MgO-Al2O3-SiO2-H2O-TiO2-Fe2O3.

Journal of Metamorphic Geology, *18*(5), 497-511. https://doi.org/10.1046/j.1525-1314.2000.00269.x

Whitmeyer, S. J., & Karlstrom, K. E. (2007). Tectonic model for the Proterozoic growth of North America. *Geosphere*, *3*(4), 220-259. https://doi.org/10.1130/GES00055.1

Yorath, C. J., Sutherland Brown, A., & Massey, N. W. D. (1999). LITHOPROBE, southern Vancouver Island, British Columbia. *Geological Survey of Canada*, *Open File 498*. https://doi.org/10.4095/210350

Zumsteg, C. L., Himmelberg, G. R., Karl, S. M., Haeussler, P. J., (2003). Metamorphism within the Chugach accretionary complex on southern Baranof Island, southeastern Alaska. *Special Papers-Geological Society of America*, *371*, 253-267. https://doi.org/10.1130/0-8137-2371-X.253

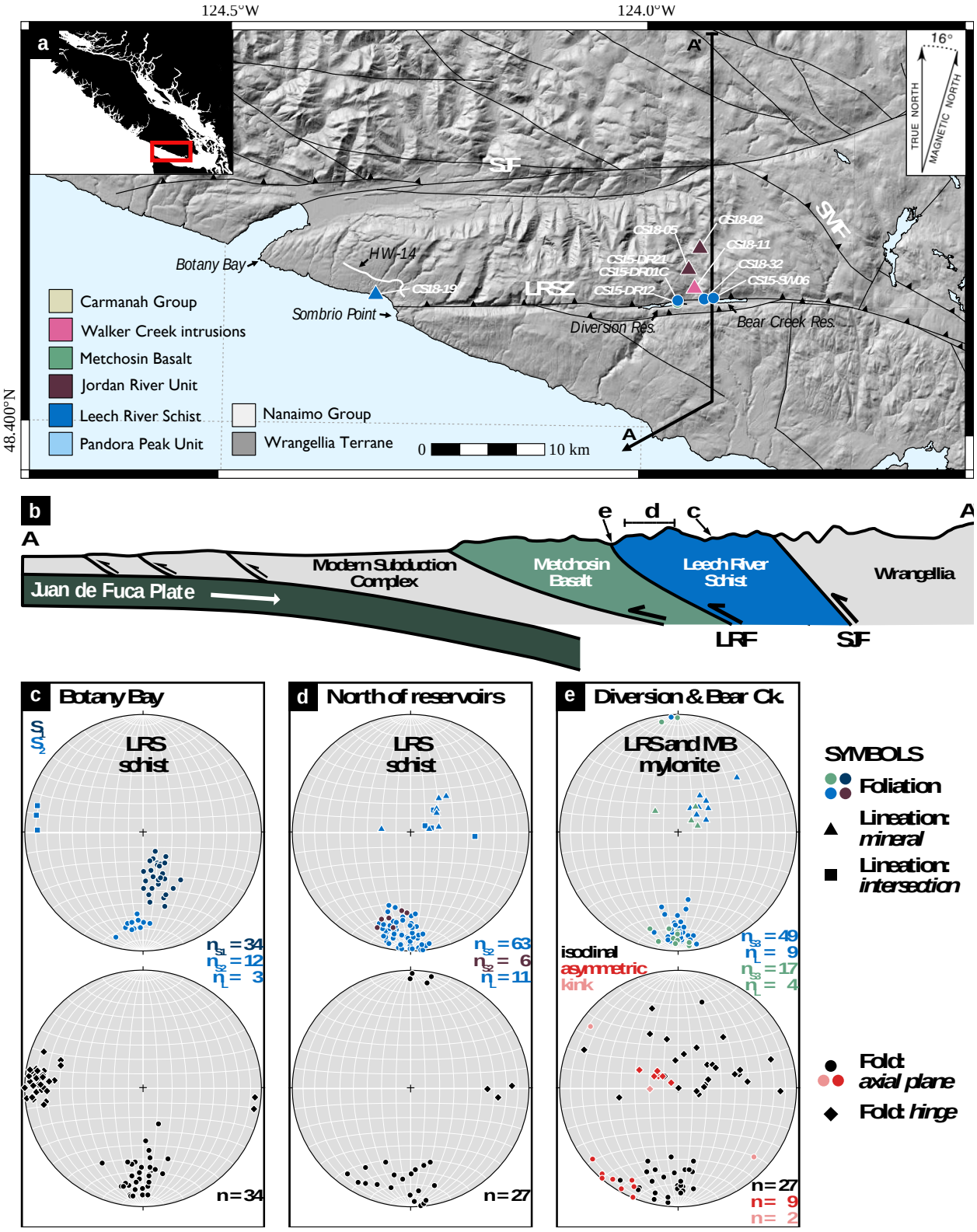


Figure 1. Geologic map, cross-section, and structural data. a) Simplified geologic map of southern Vancouver Island (adapted from Cui et al., 2017; Groome et al., 2003; Muller, 1980;

Rusmore, 1982). Locations labelled with black arrows indicate field sites. Circles and triangles represent locations of samples collected for petrography and U-Pb zircon geochronology, respectively, with colors corresponding to the sampled units. LRSZ—Leech River Shear Zone; SJF—San Juan Fault; SMF—Survey Mountain Fault. **b)** Simplified geologic cross-section (adapted from Clowes et al., 1987; Hyndman et al., 1990). Stereonet projections of foliation, lineation, and fold orientations: **c)** Foliation, lineation, and fold orientations in the Leech River Schist near Botany Bay (~0.5 km^2 area); **d)** Foliation, lineation, and fold orientations within the Leech River Schist directly north of the Diversion and Bear Creek reservoirs (up to ~2 km north of the LRSZ); **e)** Foliation, lineation, and three sets of fold orientations within the Leech River Schist and Metchosin Basalt mylonites (~12 km along strike within the shear zone). Note that isoclinal folds with shallowly plunging hinges are underrepresented due to lack of subvertical exposures. Foliation planes and fold axial planes are plotted as poles to the planes. Structural field data can be obtained in Table S2.

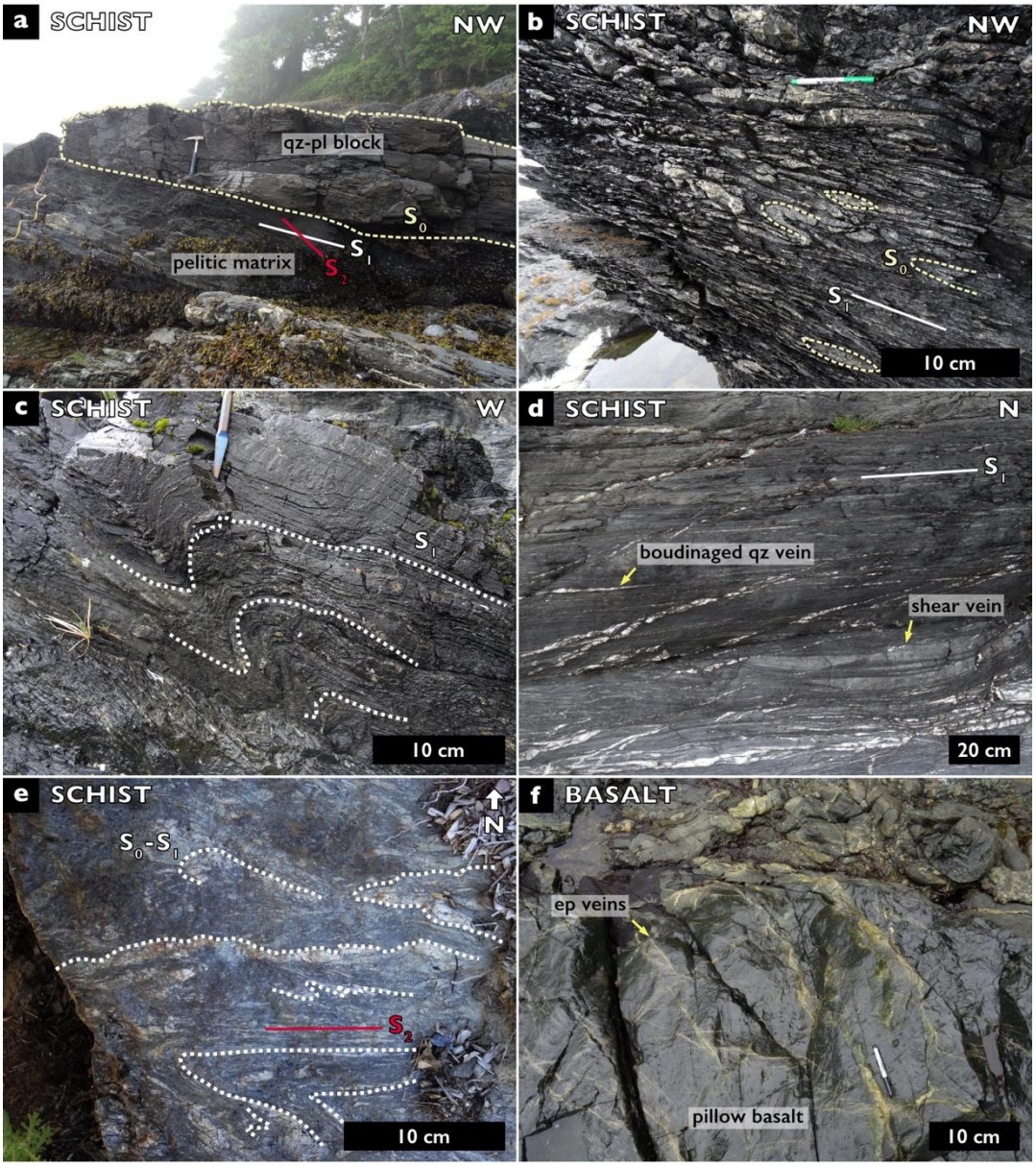
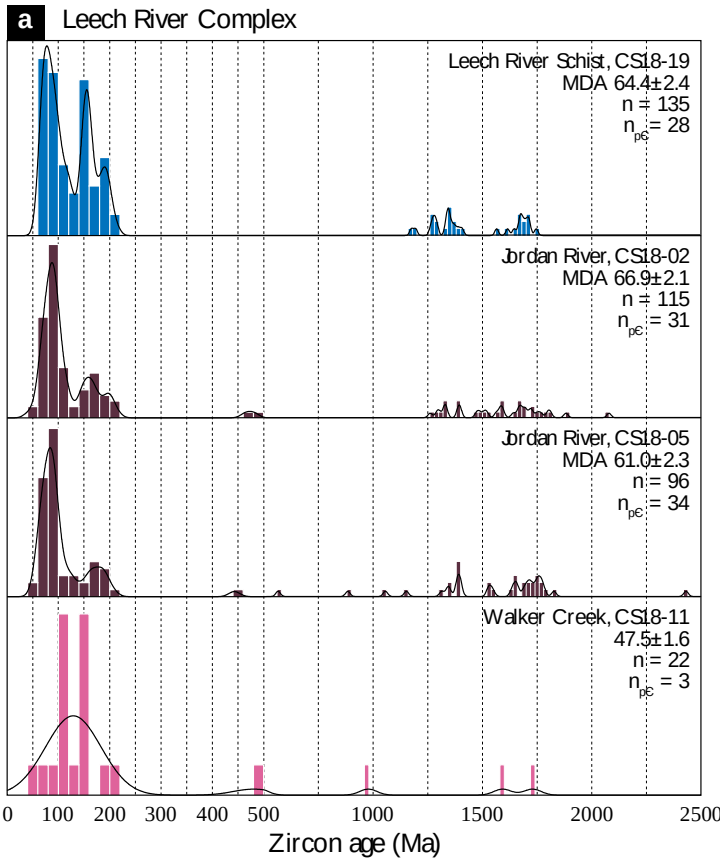
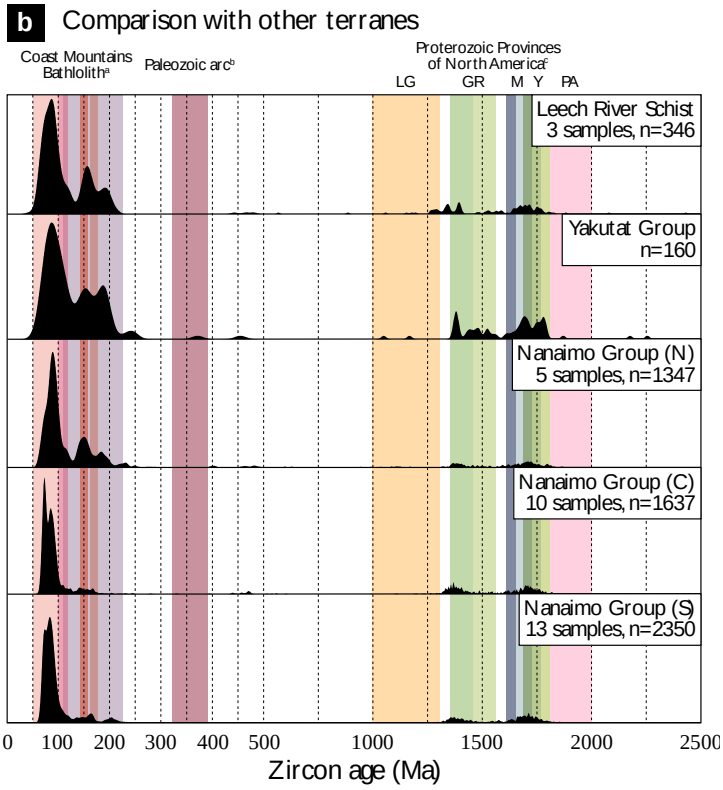


Figure 2. Field photos of structures in the hanging wall and footwall. Photos are from Botany Bay **(a-d)**, north of the Diversion and Bear Creek reservoirs **(e)**, and Sombrio Point **(f)**. **a)** Leech River Schist at Botany Bay contains centimeter- to meter-scale quartz-plagioclase blocks within a phyllosilicate-rich matrix, which defines a block-in-matrix texture and preserves original bedding (S_0) between sandstone layers and shale. The matrix has two foliation orientations (S_1 and S_2), with S_1 subparallel to the long axes of blocks. **b)** Isoclinal folding of the $S_{0\text{-}1}$ foliation with subparallel axial planes. **c)** Asymmetric, disharmonic folding of the S_1 foliation with axial planes subparallel to the S_2 foliation. **d)** Quartz veins within the LRS are oriented 0-30° from the S_1 foliation. Some shear veins host small amounts of displacement, while the veins subparallel to

foliation are offset along S_1. **e)** Leech River Schist directly north of the Diversion and Bear Creek reservoirs is composed of discontinuous quartz-plagioclase layers and micaceous layers. The S_0-S_1 foliation is transposed into parallel with the dominant S_2 foliation and tightly folded into disharmonic and often asymmetric folds. **f)** Metchosin Basalt at Sombrio Point contains pillow basalts with abundant epidote veins.


a
Leech River Complex
Leech River Schist, CS18-19
MDA 64.4±2.4
n = 135
n_pC = 28
Jordan River, CS18-02
MDA 66.9±2.1
n = 115
n_pC = 31
Jordan River, CS18-05
MDA 61.0±2.3
n = 96
n_pC = 34
Walker Creek, CS18-11
47.5±1.6
n = 22
n_pC = 3
0
100
200
300
400
500
1000
1500
2000
2500
Zircon age (Ma)


b
Comparison with other terranes
Coast Mountains Batholith[a]
Paleozoic arc[b]
Proterozoic Provinces of North America[c]
LG
GR
M
Y
PA
Leech River Schist
3 samples, n=346
Yakutat Group
n=160
Nanaimo Group (N)
5 samples, n=1347
Nanaimo Group (C)
10 samples, n=1637
Nanaimo Group (S)
13 samples, n=2350
0
100
200
300
400
500
1000
1500
2000
2500
Zircon age (Ma)

1067

Figure 3. U-Pb detrital zircon geochronology of the Leech River Complex. a) Histograms and kernel density estimates for detrital zircons from the Leech River Schist (CS1819, blue), Jordan River metasandstone (CS1802 and CS1805, purple), and the Walker Creek intrusions (CS1811, pink). Note that there is a break in scaling on the x-axis at 500 Ma, but the bin size is consistently 20 My. **b)** Detrital zircon age distributions (KDEs) from the Leech River Schist compared with the Yakutat Group (Garver & Davidson, 2015) and "Facies 2" zircons from the Upper Nanaimo Group (northern, central, and southern transects of Coutts et al., 2020; Englert et al., 2018; Matthews et al., 2017). Colored bars represent detrital zircon provenances from [a]Gehrels et al. (2009), [b]Nelson and Colpron (2007), and [c]Whitmeyer and Karlstrom (2007). LG—Llano-Grenville province. GR—Granite-Rhyolite province. M—Mazatzal province. Y—Yavapai province. PA—Paleoproterozoic arcs.

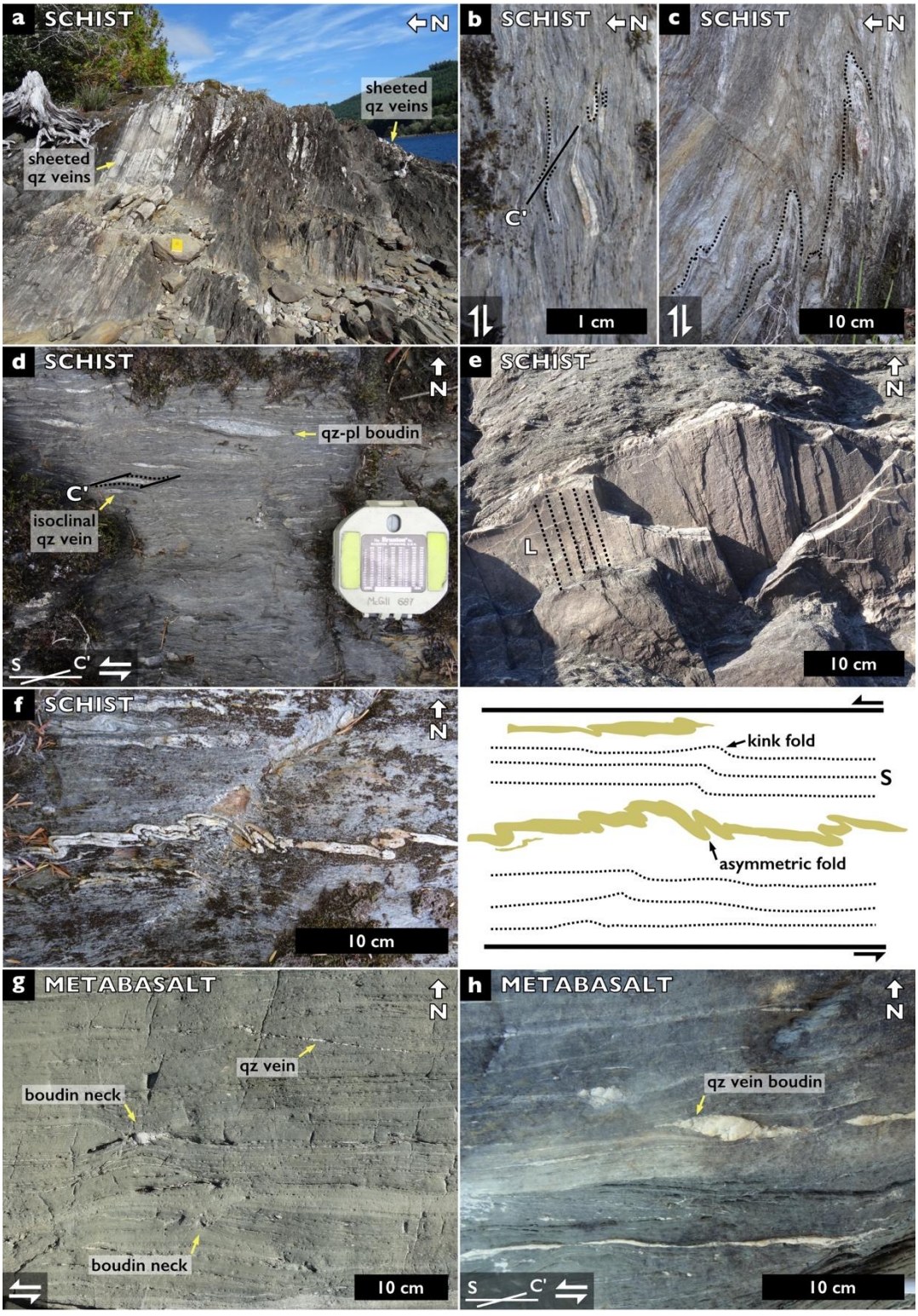


Figure 4. Field photos of structure and kinematics of the mylonite zone. Subvertical sections contain north-side-up shear sense indicators and subhorizontal sections contain left-lateral shear sense indicators. **a-c)** Subvertical sections of the Leech River Schist mylonite showing foliation

defined by compositional layering and alignment of phyllosilicate basal planes, C' shear bands, isoclinal folding of quartz-dominated layers, and asymmetric folding of the foliation. **d)** Subhorizontal section of the LRS mylonite showing foliation, C' shear bands, boudinage of quartz- and plagioclase-dominated layers, and isoclinal folding of quartz-dominated layers. **e)** Steeply plunging stretching lineation (L) visible on foliation planes within the LRS mylonite is defined by aligned mineral aggregates of phyllosilicates. **f)** Subhorizontal section of the LRS mylonite showing asymmetric shear folding of a quartz- and plagioclase-dominated layer and kink folding of foliation (S). The schematic cartoon illustrates the two types of folds. **g-h)** Subhorizontal sections of Metchosin Basalt mylonite showing foliation defined by compositional layering, C' shear bands, and boudinage of compositional layering and quartz veins.

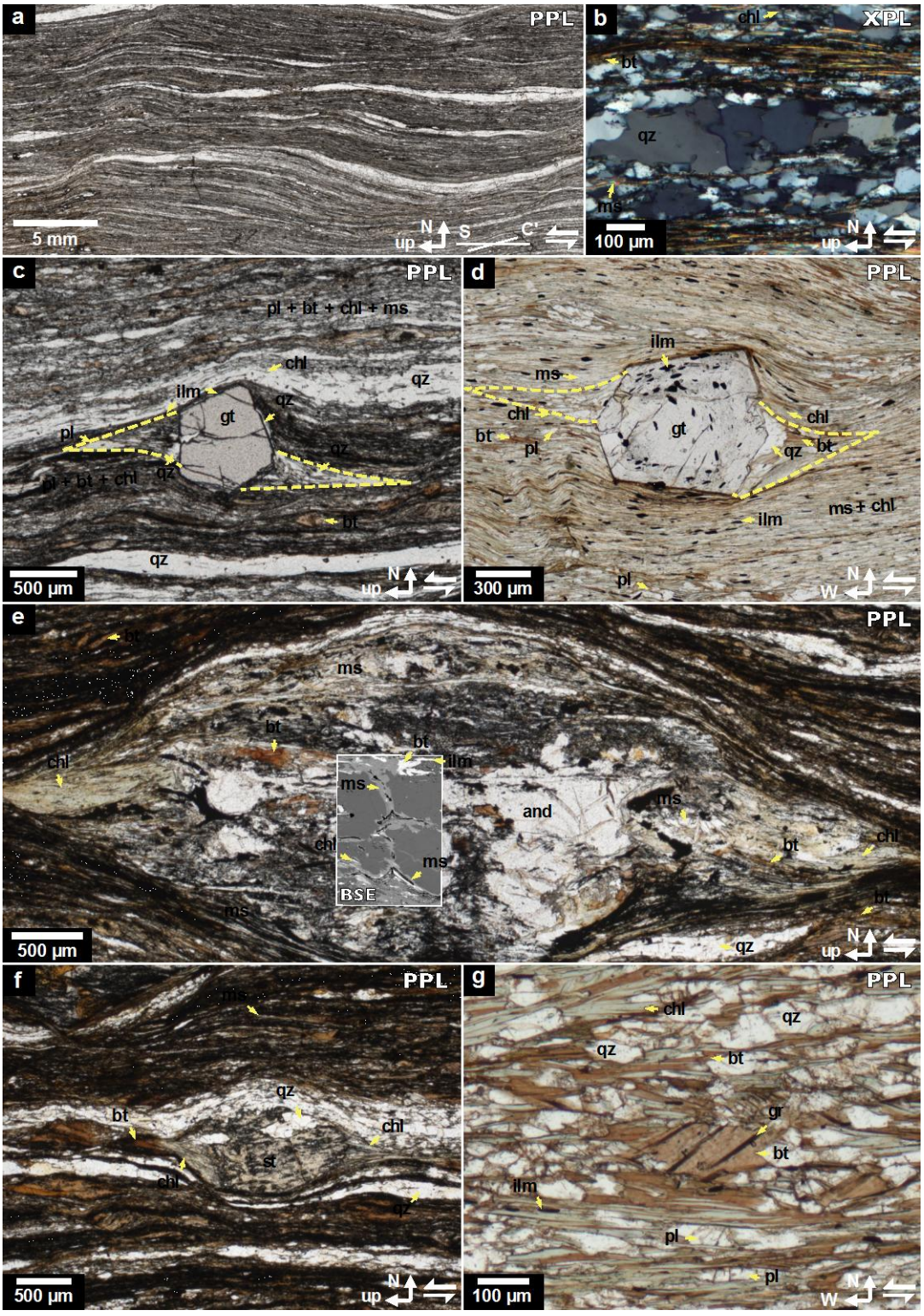


Figure 5. Leech River Schist mylonite microstructure. Photomicrographs in plane-polarized (PPL) and cross-polarized (XPL) light. **a)** Foliation planes (S) defined by compositional layering deflected by C' shear bands creating an asymmetric composite foliation. **b)** Quartz-dominated

layer with interlobate quartz grain boundaries. **c)** Garnet sigma-clast with asymmetric tails in lineation-parallel section. **d)** Garnet sigma-clast with asymmetric tails and rotated ilmenite inclusions in lineation-perpendicular section. **e)** Andalusite sigma-clast partially replaced by muscovite with asymmetric tails. **f)** Staurolite sigma-clast partially replaced by chlorite with asymmetric tails. **g)** Biotite porphyroblast with graphite inclusions and intergrown biotite and chlorite in a phyllosilicate-dominated layer. and—andalusite, bt—biotite, chl—chlorite, gr—graphite, gt—garnet, ilm—ilmenite, ms—muscovite, pl—plagioclase, qz—quartz, st—staurolite.

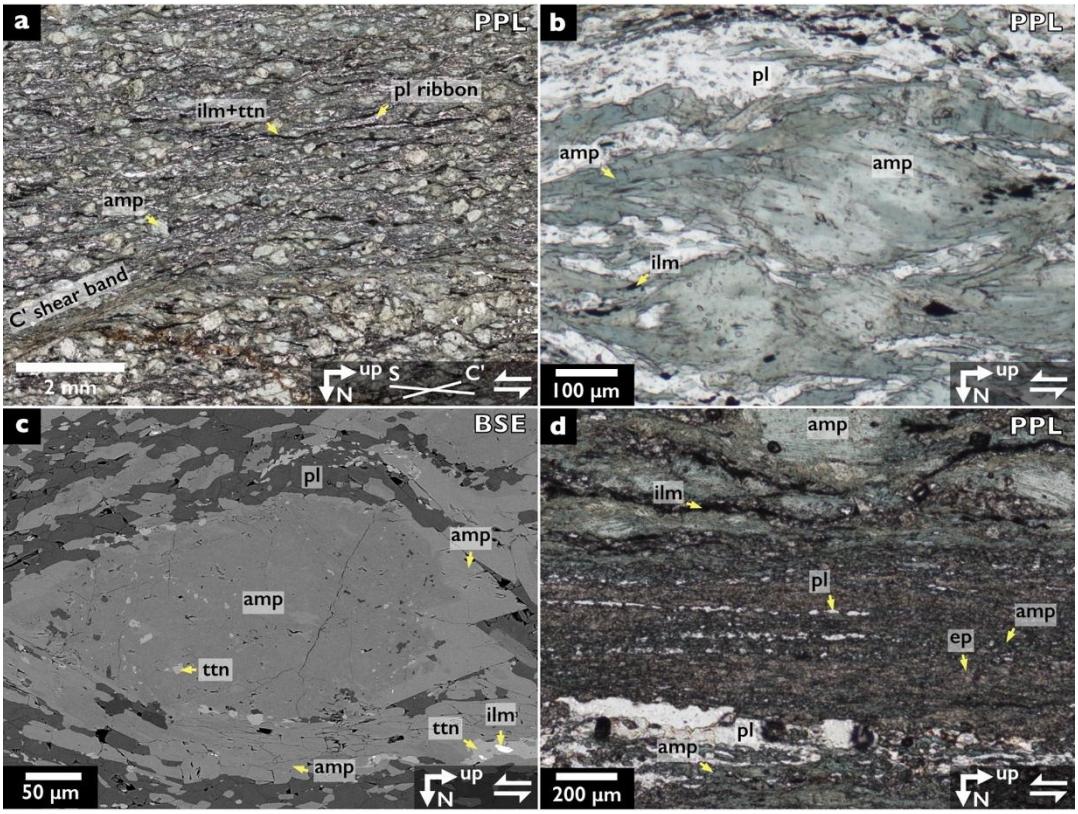


Figure 6. Metchosin Basalt mylonite microstructure. Photomicrographs in plane-polarized (PPL) and cross-polarized (XPL) light. **a)** Foliation planes (S) deflected by both C planes, oriented horizontally, and C' shear bands creating an asymmetric composite foliation. **b-c)** Chemical zoning between light green and dark green amphibole cores and tails. Fine-grained plagioclase surrounding amphibole porphyroblasts. Ilmenite seams along edges of amphibole domains. **d)** Fine-grained epidote-amphibole layer. amp—amphibole, ep—epidote, ilm—ilmenite, pl—plagioclase, ttn—titanite.

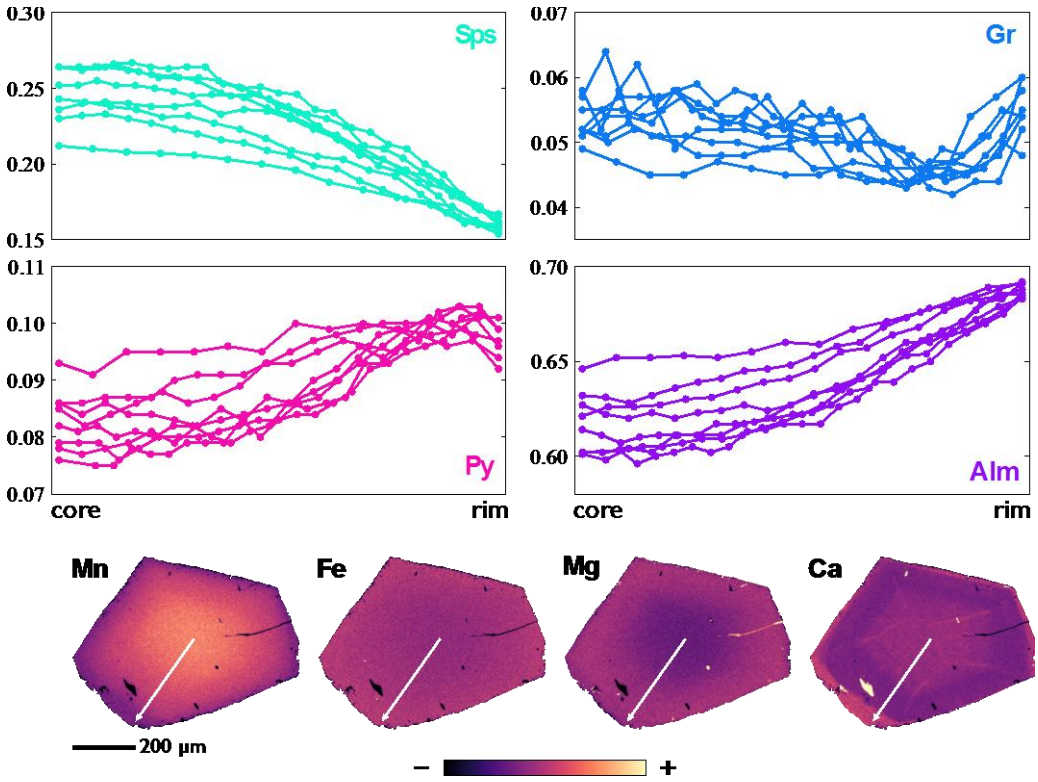


Figure 7. Garnet compositions from the schist mylonite. Garnet end-member fractions along core-to-rim transects (**top**) and representative wavelength-dispersive X-ray spectroscopy (WDS) maps (**bottom**) show garnet compositional zoning. In the cores and mantles, Mn and Ca content decreases and Mg and Fe content increases during growth. Then, in the rims, Ca and Mg content show a sharp change in thin, asymmetric rims. White arrows indicate location of microprobe transect. Sps—spessartine (Mn); Py—pyrope (Mg); Alm—almandine (Fe); Gr—grossular (Ca).

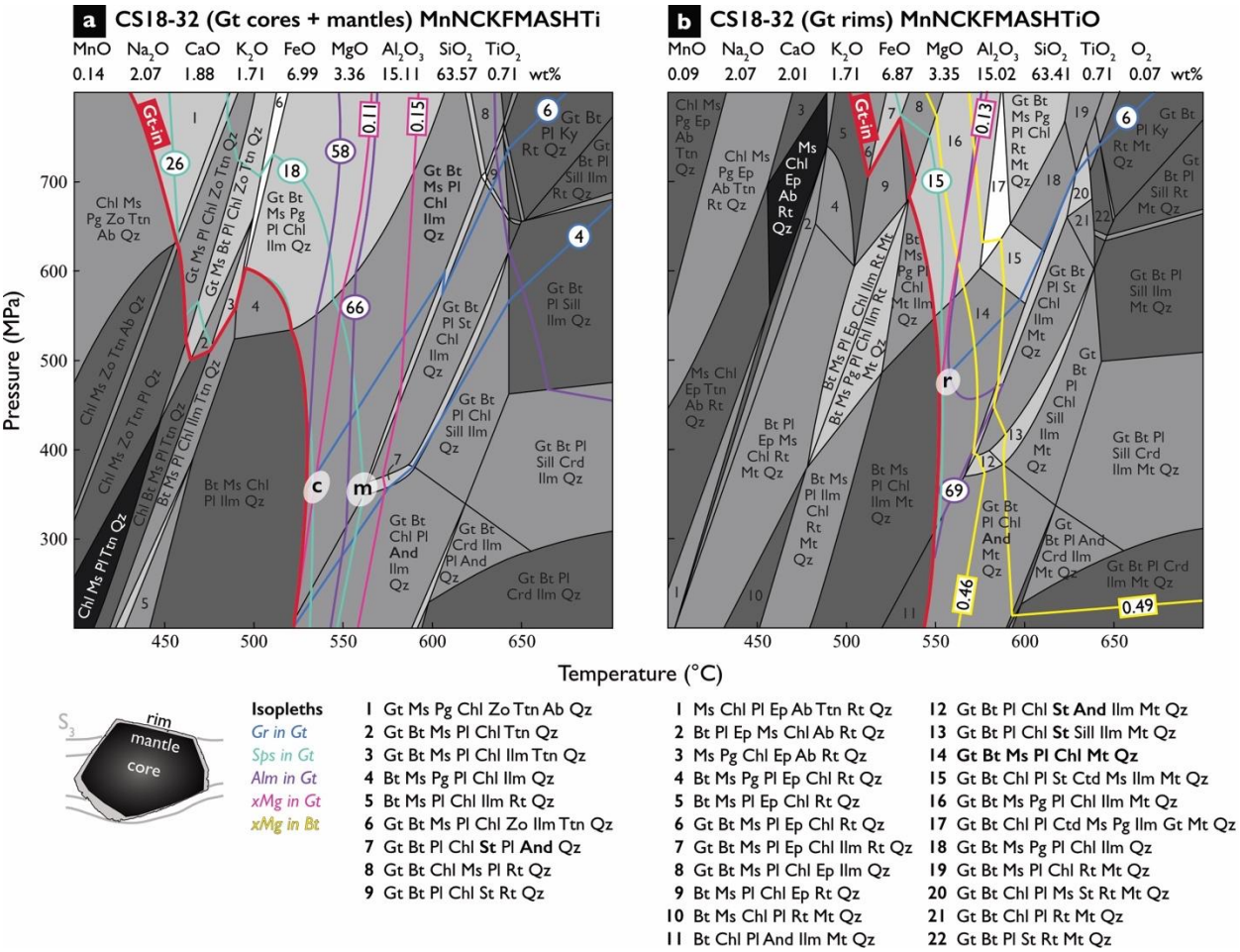


Figure 8. P-T section for schist mylonite. P-T sections generated for schist mylonite sample CS18-32 with contours of grossular (Gr), spessartine (Sps), and almandine (Alm) content as well as X_{Mg} for garnet core, mantle, and rim compositions. **a)** Garnet core compositions crossover at 525–540 °C and 340–370 MPa, while mantle compositions crossover at 550–565 °C and 340–370 MPa. **b)** Garnet rim compositions crossover at 550–570 °C and 450–490 MPa. Garnet cartoon illustrating the mylonitic foliation orientation and compositional zoning that defines the cores, mantles, and rims. Ab—albite, And—andalusite, Bt—biotite, Chl—chlorite, Crd—cordierite, Ep—epidote, Gt—garnet, Ilm—ilmenite, Ky—kyanite, Mt—magnetite, Pg—paragonite, Pl—plagioclase, Qz—quartz, Rt—rutile, Sill—sillimanite, St—staurolite, and Ttn—titanite.

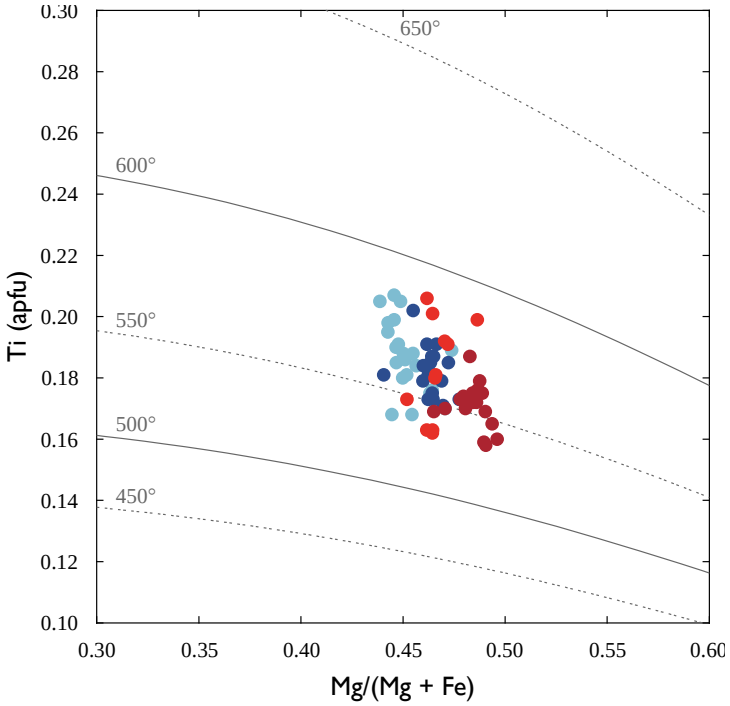
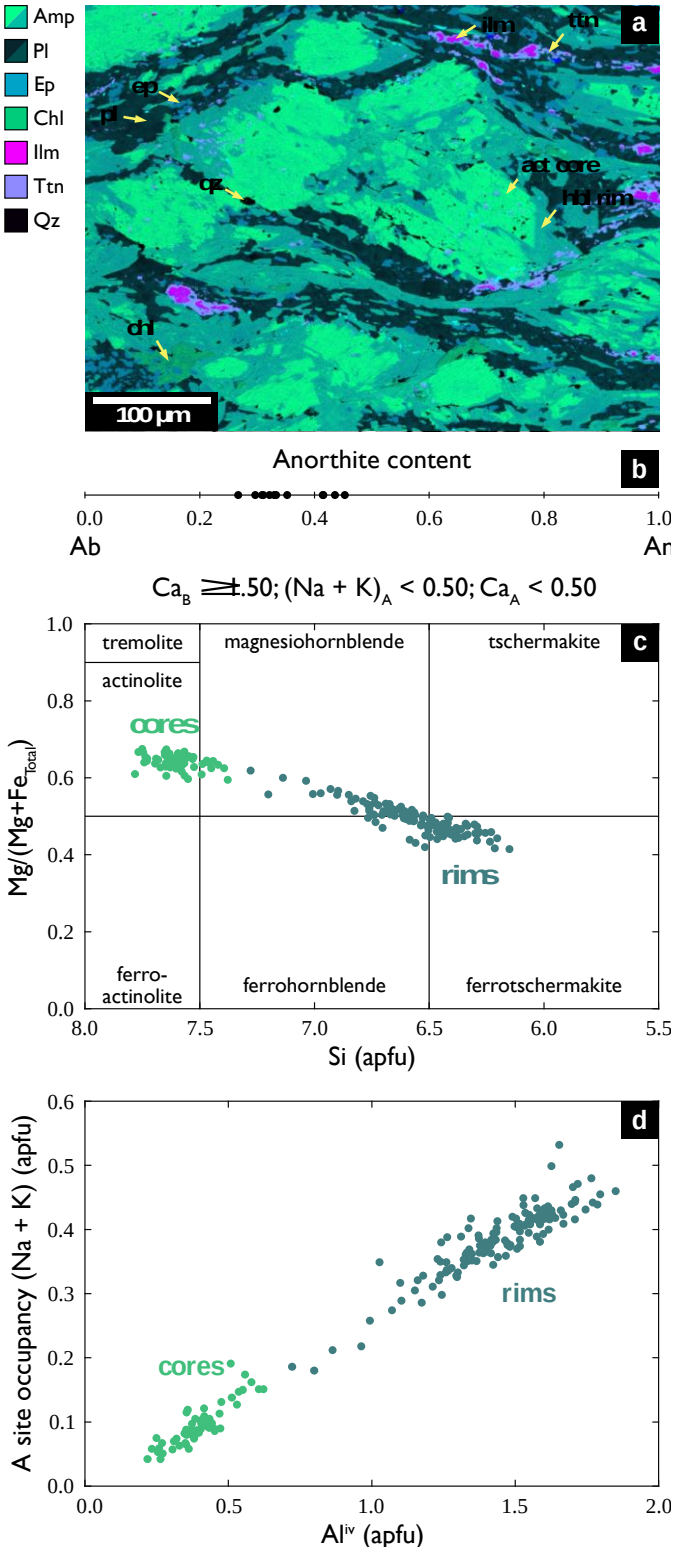


Figure 9. Ti-in-biotite thermometry. Ti content in biotite from the schist mylonite plotted on the Ti saturation surfaces of Henry et al. (2005). All analyses fall between the 500 and 600 °C contours.

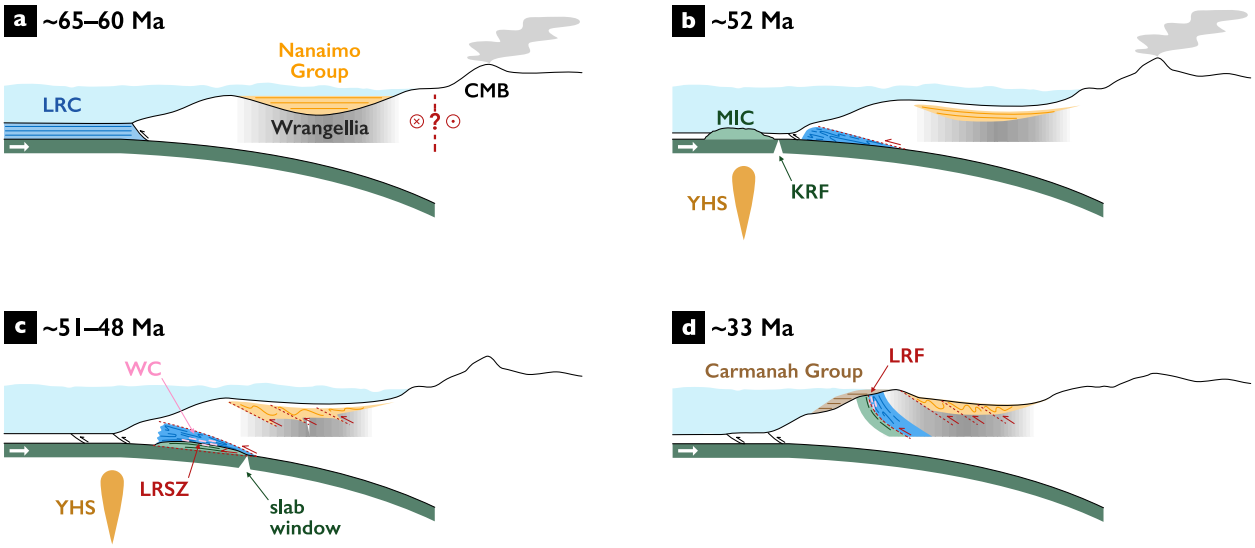


1135

1136 **Figure 10. Amphibole and plagioclase compositions from the metabasalt mylonite.**

1137 Chemical maps and point analyses from plagioclase grains and amphibole grains with chemically

distinct cores and rims. **a)** False-colored phase map generated from multiple x-ray maps highlighting chemically distinct cores and rims. Rim compositions extend into syn-kinematic tails. **b)** Plagioclase compositions in the matrix range from An_{27} to An_{45}. **c)** Amphibole core and rim compositions plotted onto a discrimination diagram with field labels following Leake et al. (1997). Cores primarily plot as actinolite, while rims plot as hornblende to tschermakite. **d)** Temperature-sensitive A site occupancy and pressure-sensitive tetrahedral alumina content demonstrate prograde growth of amphibole.



1145

1146 **Figure 11. Tectonic history of the LRC, MIC, and LRSZ.** Schematic cartoon (not to scale) of
1147 the development of the Leech River Shear Zone and surrounding terranes from ~65 Ma to ~33
1148 Ma. **a)** Synchronous deposition of the Leech River Complex and Nanaimo Group, possibly at
1149 southern latitudes and followed by northward coast-wise translation. **b)** Formation of the MIC as
1150 an oceanic plateau on the subducting oceanic plate near the Kula/Resurrection-Farallon ridge and
1151 Yellowstone hotspot. Deformation of the LRC as part of the accretionary complex. Shallow
1152 burial of the Nanaimo Group. Subduction of the Kula/Resurrection-Farallon ridge ahead of the
1153 MIC. **c)** Deformation within the LRSZ accommodating subduction of the MIC beneath the LRC,
1154 slab window formation and emplacement of the Walker Creek intrusions, and formation of the
1155 Cowichan Fold-and-Thrust belt. **d)** Exhumation of the LRC and MIC to the surface where the
1156 Oligocene-age Carmanah Group is uncomfortably deposited on top of the LRF in a coastal
1157 marine environment. CMB—Coast Mountains Batholith. KRF—Kula/Resurrection-Farallon
1158 ridge (slab window). LRC—Leech River Complex. LRF—Leech River Fault. LRSZ—Leech
1159 River Shear Zone. MIC—Metchosin Igneous Complex. WC—Walker Creek intrusions. YHS—
1160 Yellowstone Hotspot.